

2018

Fabrication, instrumentation and application for subwavelength periodic nanophotonic devices

Longju Liu
Iowa State University

Follow this and additional works at: <https://lib.dr.iastate.edu/etd>

Part of the [Electrical and Electronics Commons](#)

Recommended Citation

Liu, Longju, "Fabrication, instrumentation and application for subwavelength periodic nanophotonic devices" (2018). *Graduate Theses and Dissertations*. 16932.
<https://lib.dr.iastate.edu/etd/16932>

This Dissertation is brought to you for free and open access by the Iowa State University Capstones, Theses and Dissertations at Iowa State University Digital Repository. It has been accepted for inclusion in Graduate Theses and Dissertations by an authorized administrator of Iowa State University Digital Repository. For more information, please contact digirep@iastate.edu.

**Fabrication, instrumentation and application for subwavelength periodic
nanophotonic devices**

by

Longju Liu

A dissertation submitted to the graduate faculty

in partial fulfillment of the requirements for the degree of

DOCTOR OF PHILOSOPHY

Major: Electrical Engineering

Program of Study Committee:

Meng Lu, Major Professor

Jaeyoun Kim

Liang Dong

Rana Biswas

Jiming Song

The student author, whose presentation of the scholarship herein was approved by the program of study committee, is solely responsible for the content of this dissertation. The Graduate College will ensure this dissertation is globally accessible and will not permit alterations after a degree is conferred.

Iowa State University

Ames, Iowa

2018

Copyright © Longju Liu, 2018. All rights reserved.

DEDICATION

I would like to dedicate this dissertation to my dear parents, Ping and Juan.

TABLE OF CONTENTS

	Page
LIST OF FIGURES	v
NOMENCLATURE	viii
ACKNOWLEDGMENTS	x
ABSTRACT	xii
CHAPTER 1. INTRODUCTION	1
1.1 Motivation and Dissertation Organization	1
1.2 Key Conceptions.....	3
1.2.1 Photonic crystals and guided-mode resonance (GMR).....	3
1.2.2 Plasmonic crystals and surface plasmon resonance (SPR)	4
1.2.3 Nanoimprint lithography	5
1.2.4 Phase-change material.....	7
CHAPTER 2. GMR-BASED ANGULAR SPECTRUM DETECTION INSTRUMENT.....	10
2.1 Abstract.....	10
2.2 Introduction	10
2.3 Results and Discussions.....	16
2.4 Conclusion	19
CHAPTER 3. PROGRAMMABLE NANOREPLICA MOLDING	21
3.1 Abstract.....	21
3.2 Introduction	21
3.3 Results and Discussion	22
3.4 Conclusion.....	32
3.5 Materials and Methods	33
3.6 Acknowledgements	36
CHAPTER 4. LINEAR VARIABLE PHOTONIC FILTERS	37
4.1 Abstract.....	37
4.2 Introduction	37
4.3 Methodology.....	40
4.4 Results and Discussions.....	44
4.5 Conclusions	47
4.6 Acknowledgements	48
CHAPTER 5. PHASE-CHANGE MATERIAL FILM INCORPORATED GMR FILTER.....	49
5.1 Abstract.....	49
5.2 Introduction	49

5.3 Results and Discussion	51
5.3.1 Structure of GST-incorporated photonic crystal filter	51
5.3.2. Tuning of optical resonances of the metal-cladding	53
5.3.2.1 Tuning of GMR mode by the phase transition of GST.....	57
5.3.2.1.1 Heat-induced crystallization	59
5.3.2.1.2 Pulse laser-induced amorphization	61
5.3.2.2 Cycling between <i>a</i> -GST and <i>c</i> -GST modes	61
5.4 Conclusion	62
5.5 Experimental Section.....	63
5.6 Acknowledgements	65
 CHAPTER 6. ULTRATHIN FREESTANDING PLASMONIC MEMBRANES.....	 66
6.1 Abstract.....	66
6.2 Introduction	66
6.3 Results and Discussion	67
6.3.1 Structure of plasmonic membrane.....	67
6.3.2 Fabrication of the membrane: imprint and transfer.....	69
6.3.3 Characterization for plasmonic membrane.....	70
6.3.3.1 Transmission spectrum and EOT	70
6.3.3.2 Effect of membrane thickness on EOT	71
6.3.3.3 Angular dispersed measurement	72
6.3.4 Surface enhanced infrared absorption spectroscopy (SEIRA)	73
6.4 Conclusion	74
6.5 Experimental Section.....	75
 CHAPTER 7. CONCLUSION AND OUTLOOK.....	 77
 REFERENCES	 78

LIST OF FIGURES

	Page
Figure 1-1. (a) Prism coupling (b) Grating coupling (c) SPP excitation with phase matching.	5
Figure 1-2. Schematic of nanoimprint lithography process.....	6
Figure 1-3. Cross section diagram of the nanoreplica molding process	7
Figure 1-4. Refractive index, n and extinction coefficient, k of GST.....	8
Figure 2-1. (a) A schematic of PC structure (not to scale). (b) The complete layout of the experimental setup.....	11
Figure 2-2. Angular transmission spectra with the PC sensor immersed in DMSO-water mixture solutions with varying concentrations of DMSO from 1% to 10%.	13
Figure 2-3. Dynamic detection of resonant angle shifts for solutions with different refractive index pumped through the channel.	14
Figure 2-4. Time dependent resonant angle variation when the PC sensor was immersed in DI water.	15
Figure 2-5. Time resolved resonant angle shift due to the deposition of the alternating polyelectrolyte multilayers.	17
Figure 2-6. (a) The reconstructed USAF1951 Pattern. (b) The profile of resonant angle distribution along the three line pairs marked in (a).	18
Figure 3-1. Schematic of the programmable nanoreplica molding process.....	22
Figure 3-2. Nanopost arrays replicated using a single PDMS mold.....	24
Figure 3-3. Optical characterization of 2D plasmonic crystals.....	25
Figure 3-4. (a) The SPR reflection dips for plasmonic slabs fabricated with 0%, 2.5%, 5%, 7.5%, 10%, 15%, 20%, 25%, 30%, and 35% strain. (b) Plasmonic resonance wavelength with respect to applied strain.....	28
Figure 3-5. Reflection spectra of plasmonic crystals.....	29
Figure 3-6. Photonic band diagrams derived from the transmission spectra.	31

Figure 4-1. (a) Schematic of the linear variable replica molding process. (b) A photo showing the dimensions of the replicated wedge-shaped PDMS.....	39
Figure 4-2. (a) Schematic cross section of the PC filter structure (not to scale) and the SEM images of the replicated grating at three different positions on the sample. (b) Measured grating periods as a function of lateral position on the fabricated PC filter.....	42
Figure 4-3. Calculated transmission spectra obtained by the RCWA simulation for the graded PC filter at 11 locations spanning 20 mm with increments of 2 mm.....	44
Figure 4-4. (a) Measured transmission spectra with TE polarization at the 11 locations specified in the numerical study. (b) Dependence of measured and calculated resonant wavelengths on the lateral position.....	45
Figure 4-5. Measured transmission resonance at $x = 10$ mm with spot sizes 1 mm, 2 mm, 3 mm, and 4 mm.....	48
Figure 5-1. Grating waveguide structure with GST film.....	52
Figure 5-2. Calculated reflection spectra for GST-PC.....	54
Figure 5-3. Phase change-induced shift of resonance wavelength.	56
Figure 5-4. (a) Schematic of the optical setup for reflection measurement and laser line-scanning apparatus.	58
Figure 5-5. Measured GMR mode versus temperature.....	60
Figure 5-6. Tuning of GMR mode during six cycles of phase transitions.....	62
Figure 6-1. (a) Schematic of the freestanding plasmonic membrane (not on scale).....	67
Figure 6-2. Angular dependence of the optical transmissions and near field distributions of the FPM.....	69
Figure 6-3. Fabrication process flowchart for the freestanding plasmonic membrane.....	69
Figure 6-4. EOT spectrum at normal incidence compared with simulation	70
Figure 6-5. The effect of membrane thickness on EOT spectra	71
Figure 6-6. Angular dispersed measurement of membrane with different thickness at 5 nm, 15 nm, 25 nm and 50 nm.....	73

Figure 6-7. EOT before and after coating of copolymer. 74

Figure 6-8. Schematic of the optical characterization using FTIR for the
freestanding plasmonic membrane. 76

NOMENCLATURE

1D	One-dimensional
2D	Two-dimensional
CCD	Charge-Coupled Device
DI	Deionized
DMSO	Dimethyl Sulfoxide
EM	Electromagnetic
EOT	Extraordinary Optical Transmission
FDTD	Finite Difference Time Domain
FPM	Freestanding Plasmonic Membrane
FTIR	Fourier-Transform Infrared Spectroscopy
GMR	Guided-Mode Resonance
GST	Germanium Antimony Telluride
IR	Infrared
LVOF	Linear Variable Optical Filter
NIL	Nanoimprint Lithography
PAH	Poly(allylamine hydrochloride)
PC	Photonic Crystal
PDMS	Polydimethylsiloxane
PEI	Poly(ethylenimine)
PIC	Plasmonic Crystal
PSS	Poly(sodium 4-styrenesulfonate)
RCWA	Rigorous Coupled Wave Analysis

RIE	Reactive Ion Etching
RIU	Refractive Index Unit
SEM	Scanning Electron Microscopy
SOG	Spin-on Glass
SPR	Surface Plasmon Resonance
TE	Transverse Electric
TEC	Thermoelectric Cooler
TM	Transverse Magnetic
UV	Ultraviolet
UVCP	UV-curable polymer

ACKNOWLEDGMENTS

It is a wonderful and memorable experience pursuing a Ph.D. at Iowa State University, especially with all the lovely people around me that I would like to say “thank you” to.

First of all, I would like to convey my heartfelt gratitude to my major professor, Prof. Meng Lu, for his guidance and support through my study all the five-and-a-half years. Without him, I could not have come to ISU pursuing my dream. I think I am the luckiest one to have him as my Ph.D. advisor. He has also help me broaden my horizon and provided me with many valuable suggestions for my career. Meng is and will always be one of my best friends all my life.

Secondly, I would like to thank all members of my POS committee, Profs. Jiming Song, Liang Dong, Jaeyoun Kim and Rana Biswas for their guidance, discussions and valuable feedback on my doctoral researches and this dissertation.

Thirdly, I would like to thank all my lab mates from Laboratory of Integrated Optical Sensors, and my colleagues in 2135 Coover, with whom I have had a really pleasant and precious time in my Ph.D. life. I would like to thank Yifei Wang, Yin Huang, Le Wei, Ben Ch’ng, Dr. Yunfei Zhao, Zijian Zhao, Jiangxiang Zhang, Zhihao Liao and Hosein Monshat for making our lab a lovely and inspiring place for research. Thanks to Dr. Qiugu Wang and Dr. Zhen Xu for their insightful discussions on many interesting projects.

I would also like to thank our collaborators, Prof. Andrew. C. Hillier and his students, Russell Mahmood and Michael Johnson at CBE department, for their training and help with sputter, FT-IR, ellipsometry, profilometer and AFM measurements. I

would to thank Prof. Liang Dong at ECpE for the Nd:YAG pulse laser and the optical table used in one of my projects. I would like to thank Dr. Leung Wai at Microelectronics Research Center for his training on electron beam evaporation, scanning electron microscopy and reactive ion etching.

I would like to acknowledge U.S. National Science Foundation (NSF) and the Catron Fellowship at MRC and the Iowa State University Startup Fund for the generous support to my researches included in this dissertation.

Last, but not least, I wish to thank my family in China, my father Ping, my mother Juan and my grandparents, for their unconditional love, trust and support during all the nine years abroad. Without these I definitely cannot make it. They always care for me, but I feel sorry for the moments when I could not be there to accompany them when they need me.

ABSTRACT

This dissertation focuses on developing novel and efficient fabrication methodology for periodic nanostructures based nanophotonic devices, especially variable or tunable optical/photonic devices that based on photonic crystal or plasmonic crystal slabs. These nanophotonic devices are optically characterized to demonstrate the effectiveness. This dissertation starts by developing an angular-dispersion detection instrument based on a one-dimensional photonic crystal. This instrument was demonstrated to have applications in chemical sensing and imaging by monitoring the guided-mode resonance (GMR) supported in the PC sensor comprised of a one-dimensional grating structure. Exposed to solutions with different refractive indices or adsorbed with biomaterials, the PC sensor exhibited changes of the optical resonant modes.

In order to fabricate tunable nanophotonic devices with continuously varying resonant wavelengths, two different approaches were explored in this dissertation. The first approach is to introducing graded geometry into the structure of the device, such as a varying period over the device surface. To accomplish this, a strain-tunable soft lithography method is developed using PDMS masters as the replicate molds. The process exploits an elastomeric mold made of PDMS to generate the designed periodic pattern in a UV curable polymer (UVCP) on glass or plastic substrates. During the imprint and curing process, the PDMS mold was mechanically deformed by a uniaxial force, which causes the periodic pattern carried on the PDMS mold to vary as designed. By control the stretching direction and magnitude of the applied force carefully, the lattice constant and arrangement can be determined. For example, by stretching the mold

with a 2D array in a square lattice, rectangular and triangular lattice arrangements can be obtained. As a specific application, we have applied this programmable nanoimprint lithography method to create a linear variable photonic crystal (PC) filter with continuously tunable resonant wavelength covering a wide spectral range along its length.

The other approach is incorporating materials with tunable optical properties into the constituent material of the periodic nanophotonic devices. In this dissertation, a thin layer of phase-change material, $\text{Ge}_2\text{Sb}_2\text{Te}_5$ (GST), in nanometers was embedded in the waveguide layer of a photonic crystal (PC) structure. The PC structure is based on a one-dimensional grating with a zinc sulfide waveguide. The GST-incorporated PC (GST-PC) structure supports the guided-mode resonance (GMR) that selectively absorbs light at particular wavelengths. The tuning effects were experimentally demonstrated by the crystallization or re-amorphization of the GST thin film. The GST-PC device opens a new path for tuning optical resonances in the near infrared region. Potential applications include color generation, display, optical storage, optical switches, and optical filters.

At last, a novel fabrication method for an ultrathin freestanding gold plasmonic membrane is proposed. The freestanding plasmonic membrane was characterized using FT-IR, and demonstrated to support extraordinary optical transmission in the mid infrared wavelength range. The effect of the thickness of gold was also investigated. This plasmonic device was utilized as a surface-based optical sensor by measuring the absorption of the stretching modes of chemical bonds in the Mid-IR.

CHAPTER 1. INTRODUCTION

1.1 Motivation and Dissertation Organization

Periodic nanostructures have been playing a critical role in a wide range of optical applications. Because of its small dimension, they have the ability to control light propagation and enhance light-matter interactions¹. They are the cornerstone for photonic crystals and plasmonic crystals, since in structure, photonic crystals can be seen as periodic nanostructures with a coating of thin film of high refractive index dielectric material; while plasmonic crystals with a coating of metal thin film (assuming the periodic nanostructures themselves are dielectric). Both photonic crystals (PC) and plasmonic crystals (PIC) are now widely used because of the optical resonance supported in them. The photonic crystals are known to support the so-called guided-mode resonance (GMR), while the plasmonic crystals support the surface plasmon resonance (SPR). The optical features of these resonance are directly determined by the structure. As a result, the quality of the periodic nanostructure is crucial for the optical response.

The fabrication of subwavelength periodic nanostructures is therefore very crucial. Conventional lithography methods, including electron beam lithography, are either too expensive or low in throughput for large-scale fabrications for most laboratories. Interference lithography and nanoimprint lithography have been successfully applied to change the situation²⁻⁷. One modified nanoimprint lithography method, which uses inexpensive soft molds, is known as the soft lithography. It can provide the fabrication of periodic nanostructures with high resolution and high throughput, as well as a largely reduced cost⁸⁻¹⁰.

Soft lithography has been successful in fabrication of subwavelength periodic structures. However, it is still limited by the initial mold. The first mold used to replicate the

soft mold in soft lithography has to be fabricated by other methods, such as electron beam lithography and deep ultraviolet, which can be very expensive. Furthermore, if a feature of the pattern needs modification, a new mold has to be fabricated. In order to solve the problem and facilitate the fabrication of tunable nanophotonic devices with various patterns, a programmable nanoimprint lithography method has been developed based on soft lithography.

On the other hand, a big challenge for PC devices is to control their optical response precisely to meet specific applications. In many cases, a wide range of continuously tunable resonant wavelengths provided by a single device is highly desirable. To address such problem, researchers has developed various approaches. One approach is to introduce varying geometries in the PC device structure, where the periodicity or waveguide thickness are modulated over the device surface^{11,12}. Another approach is incorporating tunable materials, such as liquid crystal to change local refractive index, so that the spectral signature of GMR modes can be modulated^{13,14}. For example, liquid crystal has been used to tune the GMR modes but the tuning requires a few milliseconds due to the slow alignment of liquid crystal molecules.

In this dissertation, I will first introduce a few key concepts extensively used in this work in Chapter 1, including the Photonic Crystals and GMR, Plasmonic Crystals and SPR, Nanoimprint Lithography and Phase-Change Materials.

In Chapter 2, an angular detection instrument platform developed based on a 1D Photonic Crystal slab, is demonstrated as an application of periodic nanostructure-based device in chemical sensing and imaging.

In Chapter 3, a soft lithography fabrication technique is developed based on an elastomeric mold made of polydimethylsiloxane (PDMS). This technique is called Programmable Nanoimprint Lithography (PNIL), where strains are accurately applied to intentionally deform the elastomeric mold to generate various periodic lattice constants or lattice arrangements after imprinting. The effectiveness of the technique is proved using optical characterizations.

In Chapter 4, we applied the PNIL method introduced in Chapter 3 to fabricate a usable linear variable optical filter based on a photonic crystal, where the resonant wavelength is graded along the optical filter surface.

In Chapter 5 and Chapter 6, instead of introducing varying geometries into the periodic nanostructures as in Chapter 3 and Chapter 4, we inspected the possibility of incorporating one type of tunable materials, phase-change material, into the photonic crystal (Chapter 5) and plasmonic crystal (Chapter 6) to fabricate tunable nanophotonic devices, respectively.

In Chapter 7, we would conclude this dissertation and look into the future work.

1.2 Key Conceptions

During my study, I mainly works with two types of nanophotonic devices based on sub-wavelength nanostructures. One is photonic crystal (PC) slabs and the other is plasmonic devices. They both can be obtained by depositing a thin film of different materials on top of a substrate that carries a one-dimensional or two-dimensional gratings.

1.2.1 Photonic crystals and guided-mode resonance (GMR)

A photonic crystal slab can be seen as a diffraction grating and a waveguide brought into proximity. For example, it can be obtained by depositing a dielectric thin film with a relatively high refractive index onto a sub-wavelength periodic structure. Guide-mode

resonance (GMR) occurs when the diffracted mode and guided mode meet the phase-matching condition. By taking the grating equation and the ray-tracing analysis for a waveguide into account, the effective refractive index n_{eff} inside a 1D-PC can be described using Equation 1-1:

$$n_{\text{eff}} = n_1 \sin \theta_{\text{in}} - m \frac{\lambda_0}{\Lambda} \quad 1-1$$

where n_1 is the refractive index of the cladding layer, θ_{in} is the incident angle of the excitation irradiation, λ_0 is the free space wavelength of the incident light, and Λ is the periodicity of the 1D-PC. If the total internal reflection condition is satisfied, then n_{eff} can represent a leaky mode inside the 1D-PC:

$$\max[n_1, n_3] \leq n_{\text{eff}} < n_2 \quad 1-2$$

where n_1 and n_3 are the refractive indices of the cladding materials above or beneath the waveguide layer, respectively. n_2 is the refractive index of the waveguide layer.

1.2.2 Plasmonic crystals and surface plasmon resonance (SPR)

Similarly, plasmonic crystals can be defined as a sub-wavelength periodic structure with a metallic coating. They are known to support the surface plasmon resonance (SPR). In fact, metallic surface without the grating structure has also been used to initiate the surface plasmon polaritons with the help a Prism. This traditional method is called prism coupling. There are two widely known configuration of prism coupling for SPP. One is Kretschmann configuration, and the other is Otto configuration. Although these two configurations are different on whether the metal is deposited on the prism, or just positioned close enough to the prism, they share the same method of using prism as a method of phase-matching (Figure 1(b)). As can be easily understood, the prism coupling is bulky and therefore inconvenient for

a compact application. As a result, sub-wavelength periodic structures, or gratings, are used as a more compact and convenient coupling method for phase matching (Figure 1(c)).

Surface plasmon resonance (SPR) is the excitation of surface plasmon polaritons, which are electromagnetic (EM) wave propagating along a metal/dielectric interface. This special EM wave involves both the charge oscillation and the EM wave in the dielectric. When the frequency of excitation light matches the natural frequency of the oscillation of electrons inside the metal near the interface, the resonance can occur. According to Figure 1(c), for plasmonic crystals with a subwavelength grating, it can support SPR in nature. In this dissertation, SPR are all investigated using the grating coupling method.

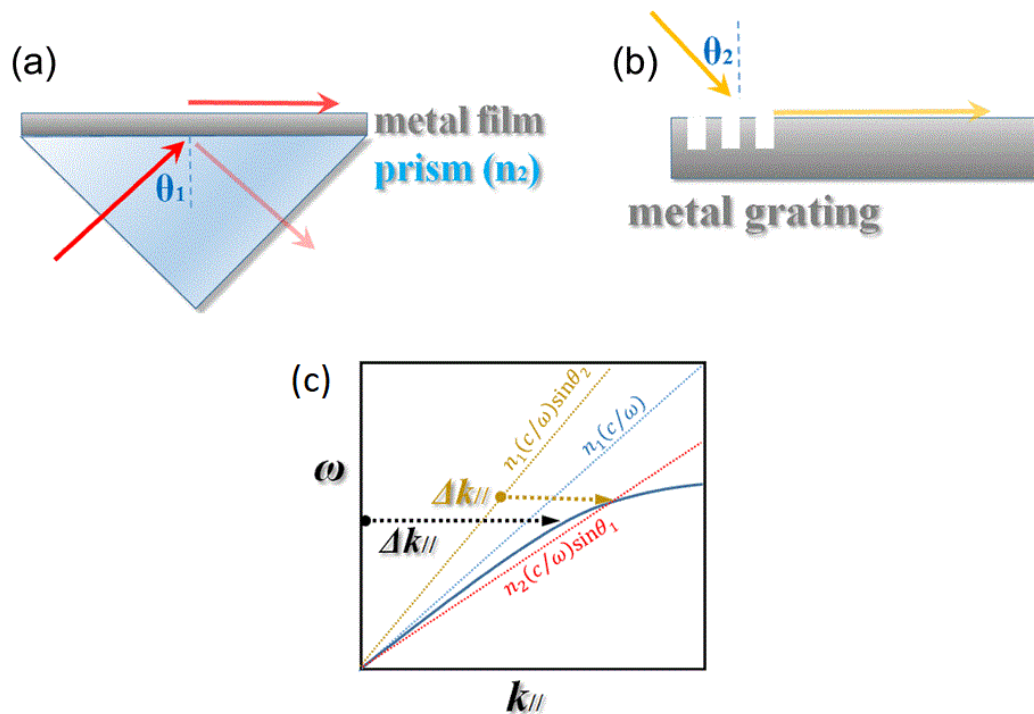


Figure 1-1. (a) Prism coupling (b) Grating coupling (c) SPP excitation with phase matching¹⁵.

1.2.3 Nanoimprint lithography

Nanoimprint lithography was invented by Steven Chou et al. in 1996². It has the advantages of high resolution, high throughput and relatively low cost, therefore it has been

adopted as the main type of fabrication method we used to transfer the periodic nanostructure pattern in this dissertation.

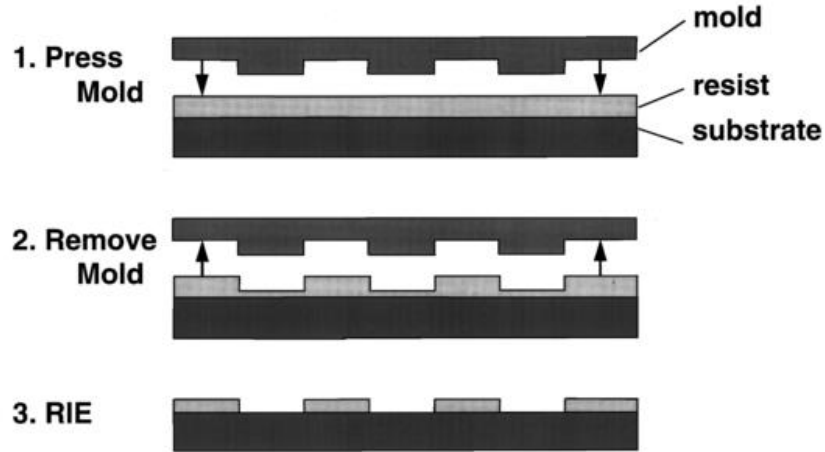


Figure 1-2. Schematic of nanoimprint lithography process²

As shown in Figure 1-2, the original nanoimprint lithography is summarized in three main steps: (1) imprint using a mold carrying the pattern to be transferred. (2) After a thickness contrast is generated in the resist, remove the mold. (3) Remove the residual layer using etching methods, usually RIE.

After its emergence in 1996, nanoimprint lithography has undergone a series of modifications. The contamination and damage to the silicon mold after each imprinting limited how many times a silicon mold can be used. Therefore, instead of using rigid molds like patterned silicon wafers, soft molds made by PDMS was used to further reduce the cost. This type of nanoimprint lithography is therefore called soft lithography for short.

The resist used in the nanoimprint lithography is usually either heat curable or photo curable, that is, can be solidified using heating or exposure to ultraviolet light (UV). The substrate can either be rigid, like silicon wafers or glass slides, or flexible, like plastic sheets.

As for the residual layer, removing it or not is depending on the specific application. In this

dissertation, we adopted the type of nanoimprint lithography, which is called nanoreplica molding, where the residual layer is not removed. We used UV curable polymer (Norland Optical Adhesive or PU) as the resist, and it is usually exposed to UV light for 5 min to fully solidify the polymer. After that, the mold is removed, and the cured polymer is patterned with the nanostructure carried on the mold. A schematic showing a typical process of the nanoreplica molding process is shown in Figure 1-3.

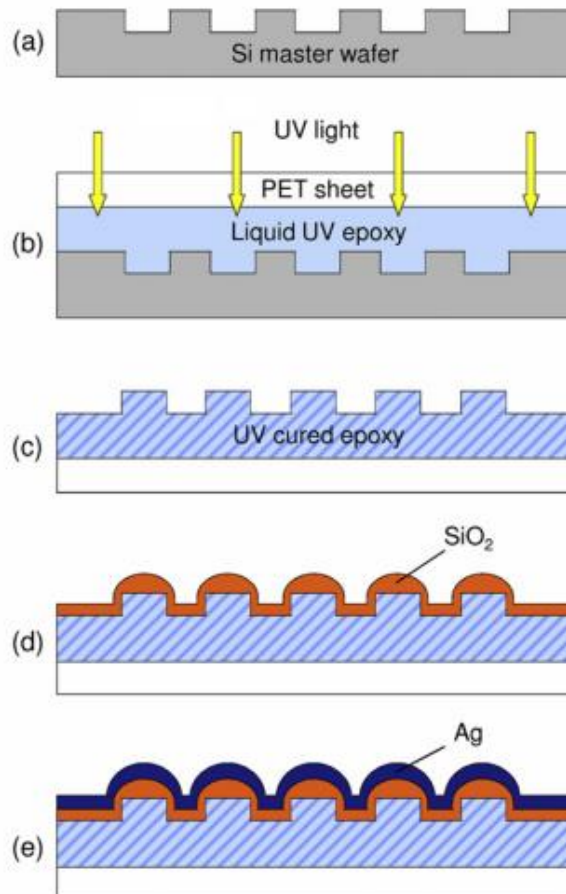


Figure 1-3. Cross section diagram of the nanoreplica molding process¹⁶

1.2.4 Phase-change material

Phase-change material is a type of material that their electrical and optical properties change greatly upon phase transitions between amorphous and crystalline states. Among

them, $\text{Ge}_2\text{Sb}_2\text{Te}_5$ (GST), the most commonly known material in germanium antimony telluride alloy family, is very famous for its non-volatile properties that are highly stable for at least 10 years in room temperature. It has attracted tons of attentions ever since its first appearance in commercial CDRWs in late 1990's. Besides the promising potential in phase-change non-volatile memory applications, GST has many attractive optical properties which makes it also desirable as an optical material in the near infrared wavelength range (NIR).

For example, GST has large contrast for both refractive index, n and extinction coefficient, k upon phase transitions between amorphous and crystalline states¹⁷, as can be seen in Figure 1-4, especially in NIR. The drastic change in the real part of the complex refractive index can be as high as 2.79 near the communication wavelength, 1550 nm. The imaginary part begins to decrease beyond 800 nm, and also drops to a relatively low level near 1550 nm for both amorphous and crystalline phase. This indicates the total loss caused by material absorption of GST has been significantly lowered around 1550 nm. These properties of n and k make GST a good candidate as an active material in the NIR.

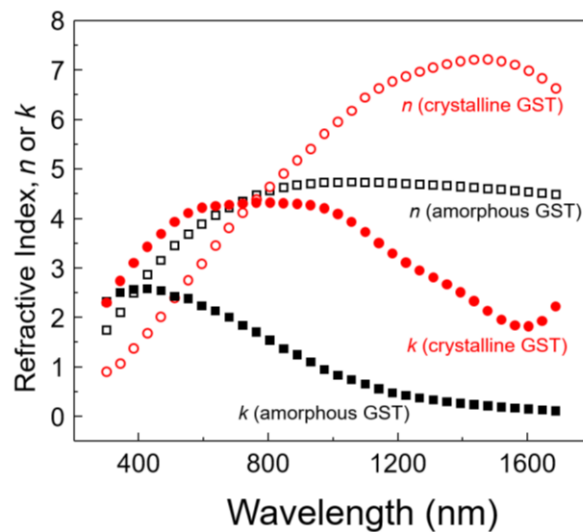


Figure 1-4. Refractive index, n and extinction coefficient, k of GST.¹⁸

In order to induce the phase transitions of GST, the energy and the duration of the stimulation source need to be precisely controlled. Researchers have already developed various methods to induce crystallization and re-amorphization of GST¹⁹.

CHAPTER 2. GMR-BASED ANGULAR SPECTRUM DETECTION INSTRUMENT

2.1 Abstract

An angular spectrum analysis system was demonstrated to monitor the optical resonant mode of a photonic crystal (PC) sensor comprised of a one-dimensional grating structure. Exposed to solutions with different refractive indices or adsorbed with biomaterials, the PC sensor exhibited changes of the optical resonant modes. The developed detection system utilized a focused laser beam to readout shifts of the resonant angle, and thereby allowed a kinetic analysis of chemical absorption. Such a detection apparatus offers an adjustable angular resolution and a tunable detection range for a wide variety of refractometric sensing applications. A limit of detection of 6.57×10^{-5} refractive index unit has been observed. The instrument also offers an imaging capability of rapidly characterizing low-contrast samples deposited on the PC surface with a spatial resolution of 10 μm .

2.2 Introduction

Label-free biosensors are an emerging class of analytic methods that are capable of quantifying biomolecular interactions, including binding affinity, specificity, and kinetics^{20,21}. Optical label-free sensors are designed as refractometric transducers that are sensitive to refractive index changes caused by the binding of target molecules. A wide variety of optical cavity based biosensors have been utilized for analyzing biomolecule and chemical compounds and have shown promising results toward rapid, high-throughput, and accurate analysis²²⁻²⁵. Among them, photonic crystal (PC) sensors have been successfully applied in life science research, pharmaceutical drug discovery, and environmental monitoring^{26,27}. They exploit leaky resonant modes, also known as guided-mode resonance (GMR), to probe refractometric variations. Each GMR mode is associated with a unique

resonant wavelength (λ_r) and resonant angle (θ_r)^{28,29}. In previous works, PC biosensors were illuminated by a white light source from a fixed angle of incidence and the reflection spectra were captured by a spectrometer to determine λ_r ³⁰.

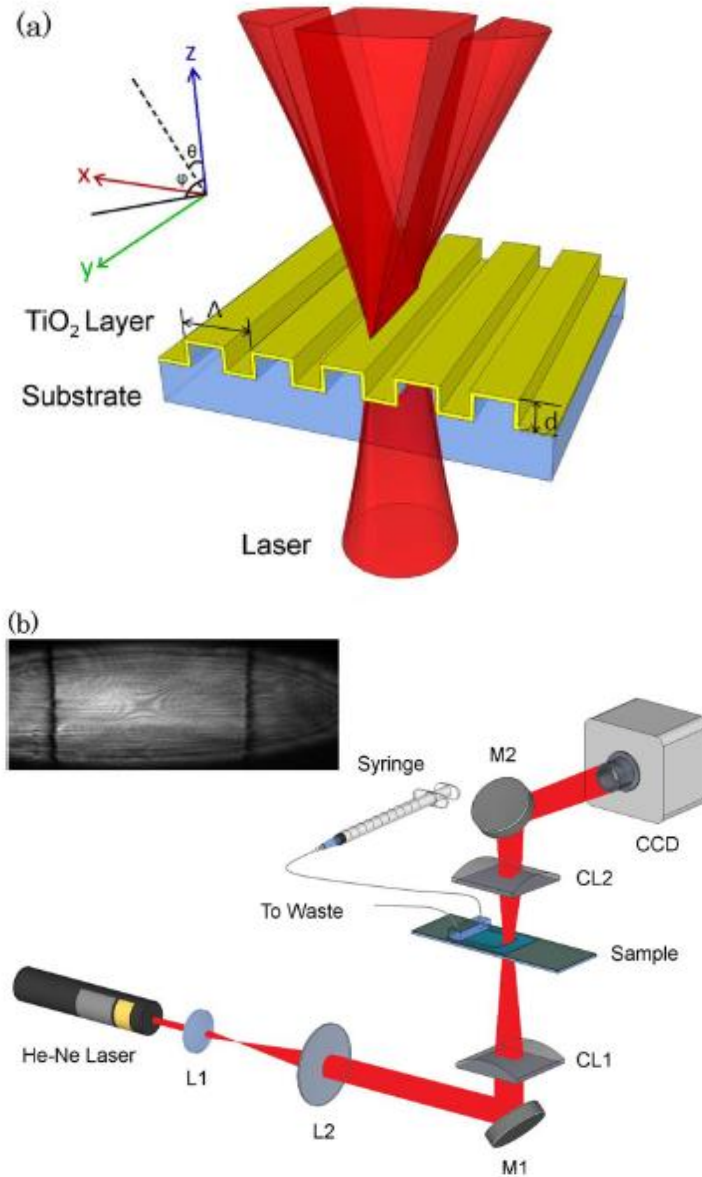


Figure 2-1. (a) A schematic of PC structure (not to scale). The grating structure was fabricated using replica-molding. (b) The complete layout of the experimental setup. The PC sensor is illuminated with an expanded He-Ne laser beam. The incoming laser light was focused along the θ -direction in the x - z plane while being collimated in the y - z plane. The transmitted light was collected by a cylindrical lens and quantified by a CCD camera. Inset: the intensity image captured by the camera showing two minimums of transmission intensity as “dark lines”.

This work reports the design of a low-cost detection instrument that utilized a line-focused laser beam to interrogate shifts in θ_r associated with a GMR, thereby enabling the rapid analysis of chemical and biomolecules absorption on a PC sensor. The performance of the developed system was characterized by monitoring the angular spectral shift in response to the refractive index change. The results showed a sensitivity of nearly 15.2° per refractive index unit (RIU), leading to a detection limit of refractive index on an order of 10^{-5} RIU. By scanning the line-focused laser beam across a region of interest and generating a spatial map of the resonant angle, this system also has the capability to quantitatively image dielectric materials of a few nanometer thickness on the PC sensor. The primary advantages of this technology include low cost, adjustable detection resolution, and tunable dynamic range.

The PC sensor adopted for this study is shown schematically in Figure 2-1(a). The low refractive index sub-wavelength grating structure was used as a cladding and light-coupling layer upon which the high reflective index dielectric layer provides a vertical light confinement. The sub-wavelength grating was fabricated using a low-cost nano-replica molding technique, which has been described previously[15]. The grating pattern was molded using a silicon master stamp (SNS-C24, LightSmyth Technologies, Inc.) with a period of $\Lambda = 416.6$ nm, a duty cycle of 50%, and a grating depth of $d = 110$ nm. After the replication using a photocurable polymer material (NOA 85, Norland Product Inc.), the surface relief grating was coated with a 100 nm thick TiO_2 dielectric film (refractive index, $n = 2.0$) by electron beam evaporation. The liquid flow chamber was fabricated by trimming a plastic paraffin film into the desired dimensions, sandwiching it between the PC substrate and a glass cover slip, and subsequently baking on a hotplate at 60°C . Two holes with

diameters of 1 mm diameter drilled in the glass cover slip served as inlet and outlet ports for flexible tubing, as shown in Figure 2-1(b).

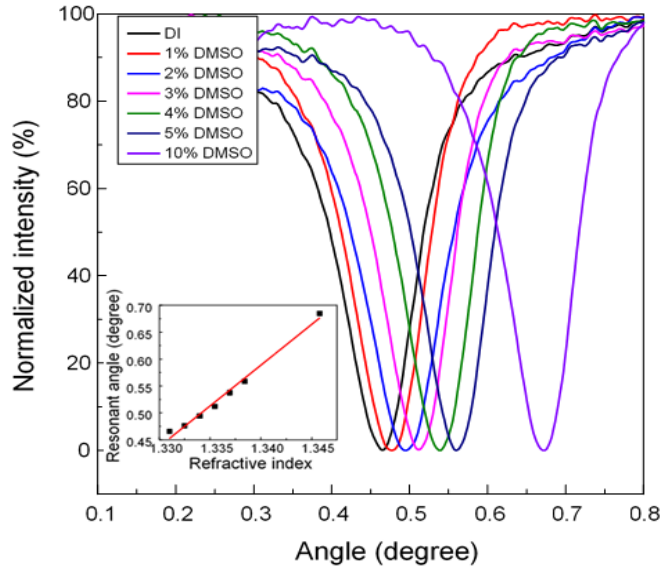


Figure 2-2. Angular transmission spectra with the PC sensor immersed in DMSO-water mixture solutions with varying concentrations of DMSO from 1% to 10%. Inset: The measured resonant angles versus the index of refraction of DMSO solutions. The measured resonant angles were fitted with a linear function shown by the red line.

A schematic of the angular dispersed detection instrument is shown in Figure 2-1(b). The system consisted of a laser source, a beam expander, two cylindrical lens (CL1 and CL2), two mirrors (M1 and M2), a sample holder, and a CCD camera. As the light source, a 0.8 mW He-Ne laser outputted a linearly polarized beam at $\lambda = 632.8$ nm. The beam was expanded using a pair of convex lens ($f_{L1} = 10$ mm and $f_{L2} = 50$ mm) to a diameter of 5 mm and was subsequently focused into a line by a cylindrical lens ($f_{CL1} = 35$ mm). At the focal plane, the laser line aligns along the y-direction, which was parallel to the direction of the PC grating (as shown in Figure 2-1(a)). In the x - z plane, the beam was focused and contained incoming rays within a range of $-8.31^\circ < \theta < 8.31^\circ$, which was limited by the numerical aperture (NA) of CL1. The focal plane of the cylindrical lens resides at the surface of the PC

sensor, which was placed on a motorized translation stage (MS-2000, Applied Scientific Instrumentation). Transmitted through the PC sensor, the laser beam diverged in the x - z plane and the intensity profile was analyzed using a CCD imaging sensor (2048×2048 pixels, $7.4 \mu\text{m} \times 7.4 \mu\text{m}$ pixel size, CoolSNAP K4, Photometrics) as illustrated in Figure 2-1(b).

Adjusting the distance between the PC sensor and the CCD offers a convenient way to tune the detection range and the sensing resolution. The second cylindrical lens (CL2, $f_{CL2} = 35$ mm) oriented orthogonally to the first cylindrical lens (CL1) and was used to project the image of the laser line onto the CCD sensor and maintain the beam path of the angularly dispersed light. This lens was optional for most experiments demonstrated in this report but required for the spatially resolved measurement.

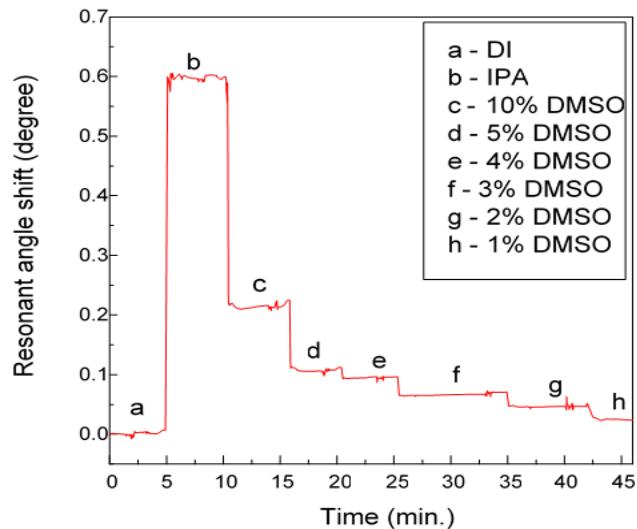


Figure 2-3. Dynamic detection of resonant angle shifts for solutions with different refractive index pumped through the channel.

By expanding and focusing the laser beam towards a PC substrate, we ensured that the angle of marginal rays was larger than θ_r of the target resonant mode. When the laser light passed through the PC sensor, the strong resonant reflection at $\pm\theta_r$ caused transmission

minima corresponding to the two resonant angles. As illustrated in the inset in Figure 2-1(b), two symmetric “dark lines” were observed on the image captured by the CCD, as a result of resonant reflection at $+\theta_r$ and $-\theta_r$, respectively. It is possible to utilize one of the lines or both to quantify the change of the resonant mode. With this intensity image, the resonant angle is determined by $\theta_r = \arctan(\Delta d/L)$, where Δd is the offset from the point of intensity minimum to the center of the optical axis, and L represents the distance between the sensor and the CCD chip. A computer program was developed to acquire intensity data from the CCD, display angular transmission spectrum, and mathematically determine the resonant angle by fitting the transmission curve with a Lorentzian profile. The amount of resonant angle shift is proportional to the refractive index change, which is usually caused by the deposition of biomaterials on the sensor surface.

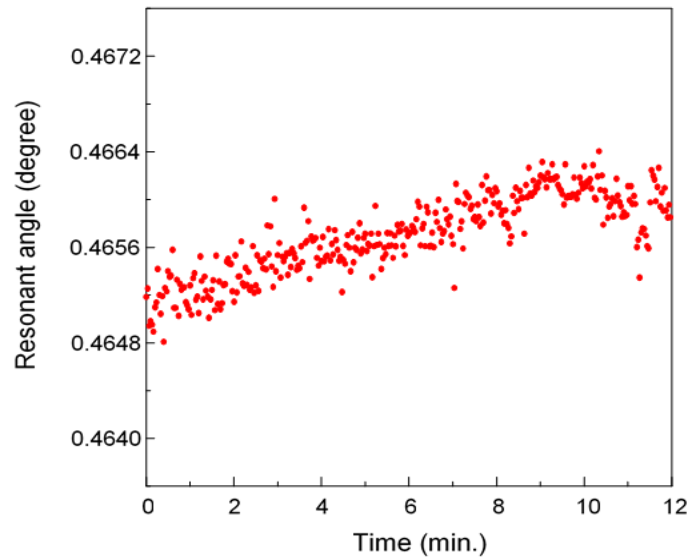


Figure 2-4. Time dependent resonant angle variation when the PC sensor was immersed in DI water.

2.3 Results and Discussions

To characterize the sensitivity of the system, different concentrations of dimethyl sulfoxide (DMSO) were loaded into the flow cell and the angular spectra from the PC sensor were measured. The DMSO was diluted in deionized (DI) water at a range of volume ratios from 1% to 10%. Figure 2-2 compares the angular transmission spectra recorded for the DMSO solution and DI water. According to the inset of **Error! Reference source not found.**, the bulk refractometric sensitivity, $S_b \equiv \Delta\theta_r/\Delta n$, was found to be 15.2°/RIU. By monitoring the angular transmission output of the PC sensor over time, the developed instrument can also be used to study dynamic characteristics. Figure 2-3 illustrates the kinetic progression of the PC resonant angle when eight different solutions flowed through the channel sequencing. The channel was rinsed with DI water ($n = 1.333$) for 5 minutes, and then isopropyl alcohol (IPA, $n = 1.377$) was introduced and caused an increase of angle shift of 0.61°. When six different DMSO solutions (10%, 5%, 4%, 3%, 2% and 1%) passed through the PC sensor, the corresponding decreasing angle shifts were recorded as shown in Figure 2-3. In order to determine the detection limit, the resonant angle was measured every 2 seconds with DI water flowing in the flow cell for a total period of 12 minutes (Figure 2-4). The resonant angle varied in a range of 1.6×10^{-3} degree with a standard deviation (σ) of 3.33×10^{-4} degree. With a minimum detectable resonant angle shift of $3\sigma = 9.99 \times 10^{-4}$ degree, the refractive index resolution was calculated as $3\sigma/S_b = 6.57 \times 10^{-5}$ RIU.

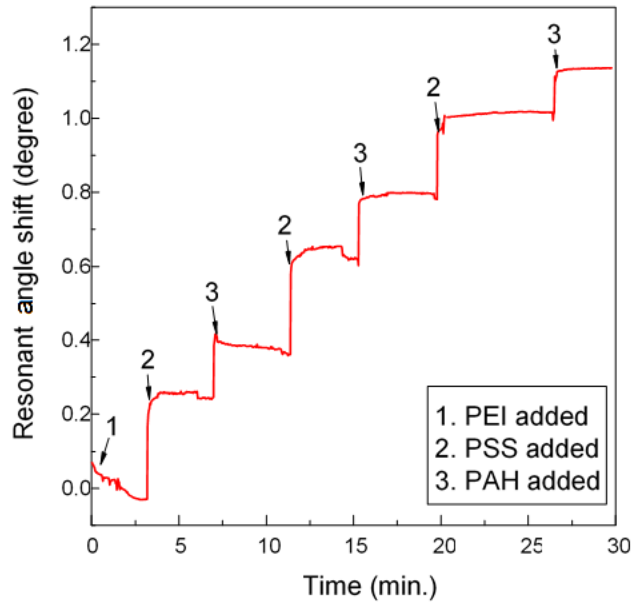


Figure 2-5. Time resolved resonant angle shift due to the deposition of the alternating polyelectrolyte multilayers.

Monitoring the resonant angle shift over time enables dynamic quantification of mass adsorption upon a PC sensor. As an example, the deposition process of a polyelectrolyte stack, which contained positively and negatively charged monolayers, was measured using the PC sensing system. Before building up the stacked layers, a 0.9 M sodium chloride (NaCl) buffer was used to establish a baseline and was subsequently replaced by a cationic poly(ethylenimine) (PEI) solution. After being incubated for 10 minutes, the flow cell was washed with NaCl buffer and three alternating layers of anionic poly(sodium 4-styrenesulfonate) (PSS) and cationic poly(allylamine hydrochloride) (PAH) were pumped into the flow cell. All polyelectrolytes were dissolved in the NaCl buffer at a concentration of 5 mg/mL and formed monolayers on the PC surface with a refractive index of 1.49 and thickness of $\sim 5 \text{ nm}$ ³¹. Figure 2-5 shows the time resolved resonant angle shift ($\theta_r \sim 1.2^\circ$)

caused by the PEI and the three PSS-PAH layers, with the measurement interval set to 2 seconds.

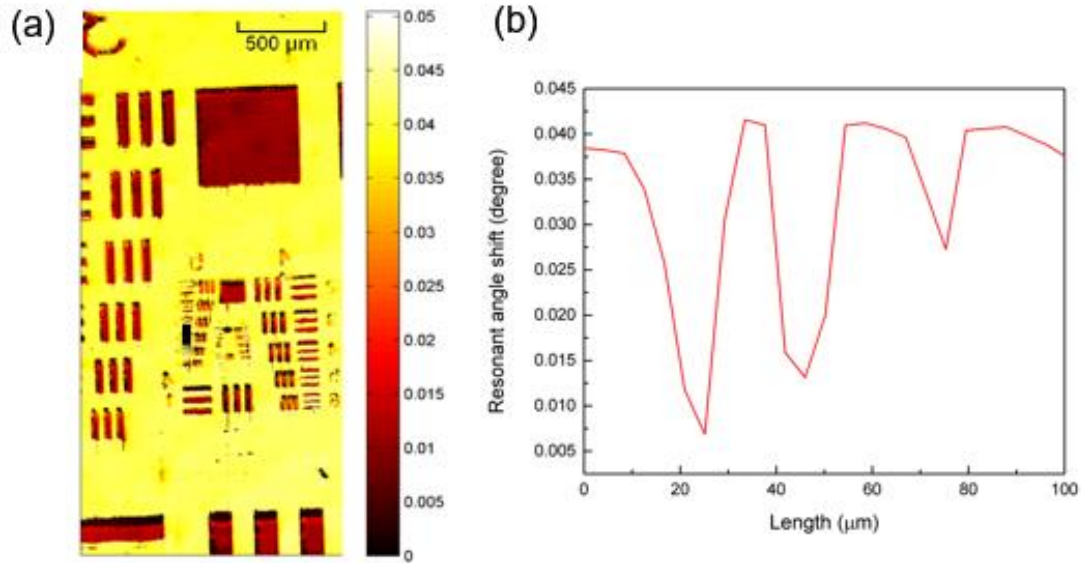


Figure 2-6. (a) The reconstructed USAF1951 Pattern. The color bar represented the angle shift of the PC sensor. (b) The profile of resonant angle distribution along the three line pairs marked in (a).

Quantification of low-contrast samples is always challenging for conventional optical imaging approaches³². Because of its high sensitivity and the spatially confined optical resonance, a PC sensor is capable of determining the density of biomaterial attachments with subtle spatial variations. Label-free detection of live cell behaviors upon a PC sensor has been successfully demonstrated in the recent work³³. The readout system shown in Figure 2-1 offers a cost effective apparatus for label-free imaging applications compared to the established method that involves expensive imaging spectrometers. To illustrate this imaging scheme, we used photolithography and lift-off process to create a low-contrast pattern (USAF1951 resolving pattern) upon the PC surface using a 5 nm TiO₂ layer deposited only in the transparent regions of the resolving pattern. The additional TiO₂ coating increased the local resonant angle by a small amount relative to the uncoated regions. By measuring the

resonant angles on a pixel-by-pixel basis over an area of interest, a map of surface absorbed mass can be generated. In order to assemble the map, a series of lines were recorded by translating the sample linearly across the laser line with a step size of $1.5 \mu\text{m}$ and an acquisition rate of 20 lines per second. Each intensity image from the CCD contained the angular spectra from 2048 pixels along the sampling line. The pseudocolor plot shown in Figure 2-6(a) consists of 1024×2048 sensing pixels and covers an area of $1536 \mu\text{m} \times 3368 \mu\text{m}$ on the PC sample. With a magnification of 4.5, each pixel in the θ_r distribution image represented an area of $1.50 \mu\text{m} \times 1.64 \mu\text{m}$ on the PC surface. A line profiled taken through the three line pairs marked in Figure 2-6(a) is shown in Figure 2-6(b). The cross-section plot showed the resonant angle contrast of $\sim 0.04^\circ$ and the minimum resolvable feature of $10 \mu\text{m}$, which was close to the diffraction limit of the cylindrical lens (CL2). The map of resonant angle distribution represented the thickness of the TiO_2 pattern, which was analogous to the absorption of biomaterials on the PC substrate.

2.4 Conclusion

In conclusion, this letter reports a low-cost detection instrument for refractometric sensing using photonic crystal biosensors. The developed detection system utilizes a focused laser beam to precisely measure changes in the resonant angle of a PC sensor. Such an optical arrangement allows flexible selection of detection range and offers adjustable angular resolution. A detection limit of 6.57×10^{-5} refractive index unit to bulk index changes and the kinetic characterization of surface-adsorbed monolayers of polymers have been demonstrated. We demonstrated its capability for quantitative mapping of a thin dielectric film patterned upon a PC sensor with a spatial resolution of $10 \mu\text{m}$. For future works, the developed technology will be applied to image biomaterials, such as an antibody and DNA

microarrays, printed on PC sensors. Due to its simplicity, the developed readout approach can also be utilized to further reduce the size of portable PC sensor systems³⁴.

This research was supported by the start-up funding from the Iowa State University.

CHAPTER 3. PROGRAMMABLE NANOREPLICA MOLDING

3.1 Abstract

The ability to fabricate periodic structures with sub-wavelength features has a great potential for impact on integrated optics, optical sensors, and photovoltaic devices. Here, we report a programmable nanoreplica molding process to fabricate a variety of sub-micrometer periodic patterns using a single mold. The process utilizes a stretchable mold to produce the desired periodic structure in a photopolymer on glass or plastic substrates. During the replica molding process, a uniaxial force is applied to the mold and results in changes of the periodic structure, which resides on the surface of the mold. Direction and magnitude of the force determine the array geometry, including the lattice constant and arrangement. By stretching the mold, 2D arrays with square, rectangular, and triangular lattice structures can be fabricated. As one example, we present a plasmonic crystal device with surface plasmon resonances determined by the force applied during molding. In addition, photonic crystal slabs with different array patterns are fabricated and characterized. This unique process offers the capability of generating various periodic nanostructures rapidly and inexpensively.

3.2 Introduction

In this work, we present various plasmonic crystals and photonic crystal slabs fabricated by a programmable nanoreplica molding process that uses a single mold. This technique uses mechanical stretching of an elastic polydimethylsiloxane (PDMS) mold to create periodic structures with various periods and lattice arrangements. At the same time, it maintains the high-throughput and low-cost features of the conventional nanoreplica molding approach. When a force is applied, the surface of the PDMS mold adjusts itself to a negative volume profile of the desired periodic structure. Replicating the stretched mold shape in a

UV-curable polymer (UVCP) yields programmable nanostructures in a process that is inexpensive and amenable to scale-up. Following replica molding, the periodic structures produced may be coated with a dielectric or thin metal film; some examples are titanium dioxide (TiO_2), gold, and silver. With a 100 nm-thick silver coating, the fabricated 2D plasmonic crystals exhibit surface plasmon resonances (SPRs) in the spectral range 410 nm to 570 nm. Using the same PDMS mold, we fabricated photonics crystal slabs with three different lattice arrangements, namely, square, rectangular, and triangular structures. The photonic crystal slabs use a 160 nm-thick TiO_2 film as the light-confinement layer. Finally, band diagrams of the fabricated photonic crystal slabs are experimentally determined and compared to simulations from electromagnetic theory.

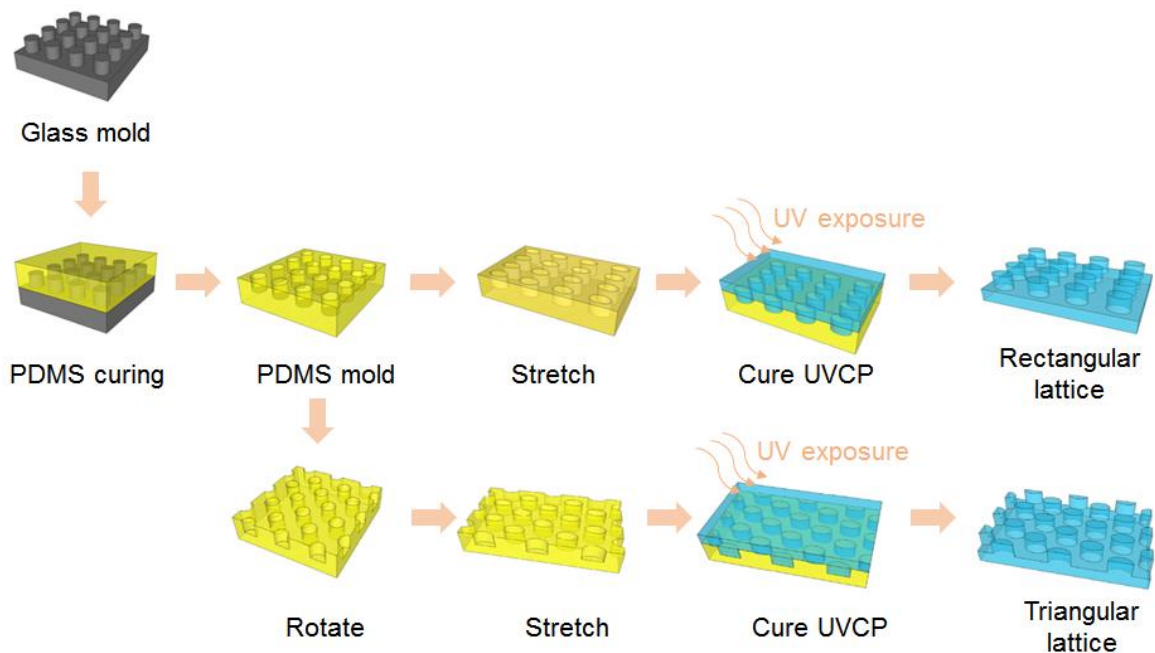


Figure 3-1. Schematic of the programmable nanoreplica molding process.

3.3 Results and Discussion

Figure 3-1 summarizes the major steps of the programmable nanoreplica molding process. The major fabrication procedures include mold preparation, mold stretching, pattern

transfer, and mold release. As the initial step, a PDMS mold is replicated from a rigid glass stamp carrying a 2D array of nanoposts with a square lattice arrangement and periods $A_x = A_y = 300$ nm. The glass stamp was produced using a glass thermal imprinting process, reported previously^{35,36}. Next, the PDMS mold is precisely stretched to obtain a lattice pattern for a particular device. A uniaxial force is applied to the PDMS mold in the plane parallel to its surface. Along the direction of the force (y -axis), the array is stretched and its period increases. Consequently, the array is also compressed in the perpendicular x -direction and the array period is reduced. Likewise, stretching the PDMS mold in other directions also allows us to program the lattice arrangement. As shown in Figure 3-1, the PDMS mold can be pulled along a diagonal direction to convert the original square lattice into a triangular lattice. From a stretched PDMS mold, the modified periodic pattern is replicated onto a glass or plastic substrate by the nanoreplica molding process. The details of the process are described below in the experimental section. Briefly, a layer of liquid UVCP material is squeezed between the stretched PDMS mold and a glass or plastic substrate. On exposure to UV illumination, the UVCP solidifies and subsequently releases from the PDMS mold.

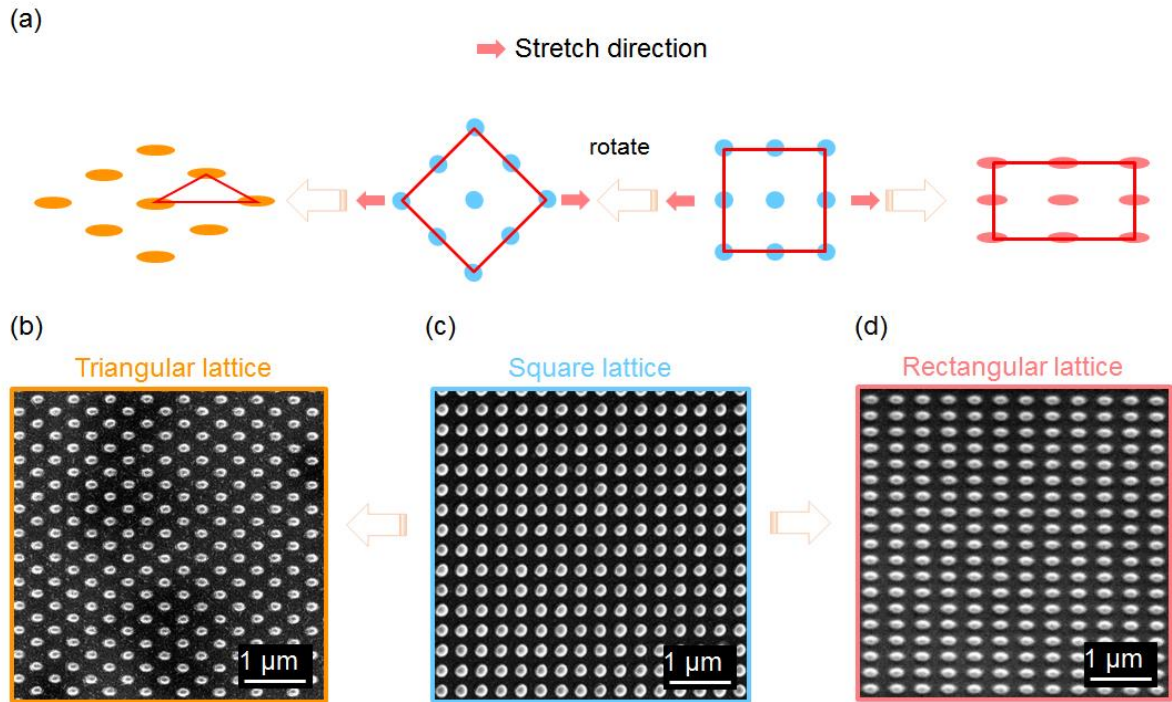


Figure 3-2. Nanopost arrays replicated using a single PDMS mold. Scheme of the mold programming process, beginning at the third figure from the left (a). SEM images of nanopost arrays with triangular lattice (b), square lattice (c), and rectangular lattice (d).

Figure 3-2 schematically illustrates how the geometry of the periodic nanostructure is tuned to produce different types of arrays. The blue dots represent the nanoposts of the unstretched square lattice with a period of 300 nm. When a uniaxial force is applied along the x -axis, the square lattice is changed to a rectangular one, as shown by the array of cherry-colored dots. Figure 3-2(b), 2(c), and 2(d) are the scanning electron microscopy (SEM) images of replicated triangular, square, and rectangular arrays, respectively. The rectangular array shown in Figure 3-2(d) was fabricated when the PDMS mold was under a strain of 40%. The period of the array increases to $A_x = 420$ nm along the direction of the applied force. The lattice shows a slight shrinkage in the direction perpendicular to the force, with a period of $A_y = 258$ nm. Meanwhile, the cross section of the nanoposts changes from circular to elliptical; however the duty cycles of the periodic structure (post size/period) remain

unchanged. When the PDMS mold is stretched along the diagonal direction, it is possible to produce periodic arrays with a triangular lattice, which is illustrated by the array of orange dots in Figure 3-2(b). Figure 3-2(b) shows the replication fabricated when the PDMS mold was under a 40% stretch along the 45° direction to the x -axis. With precise control of the degree and direction of the stretch, the triangular lattice could be tuned into a hexagonal one.

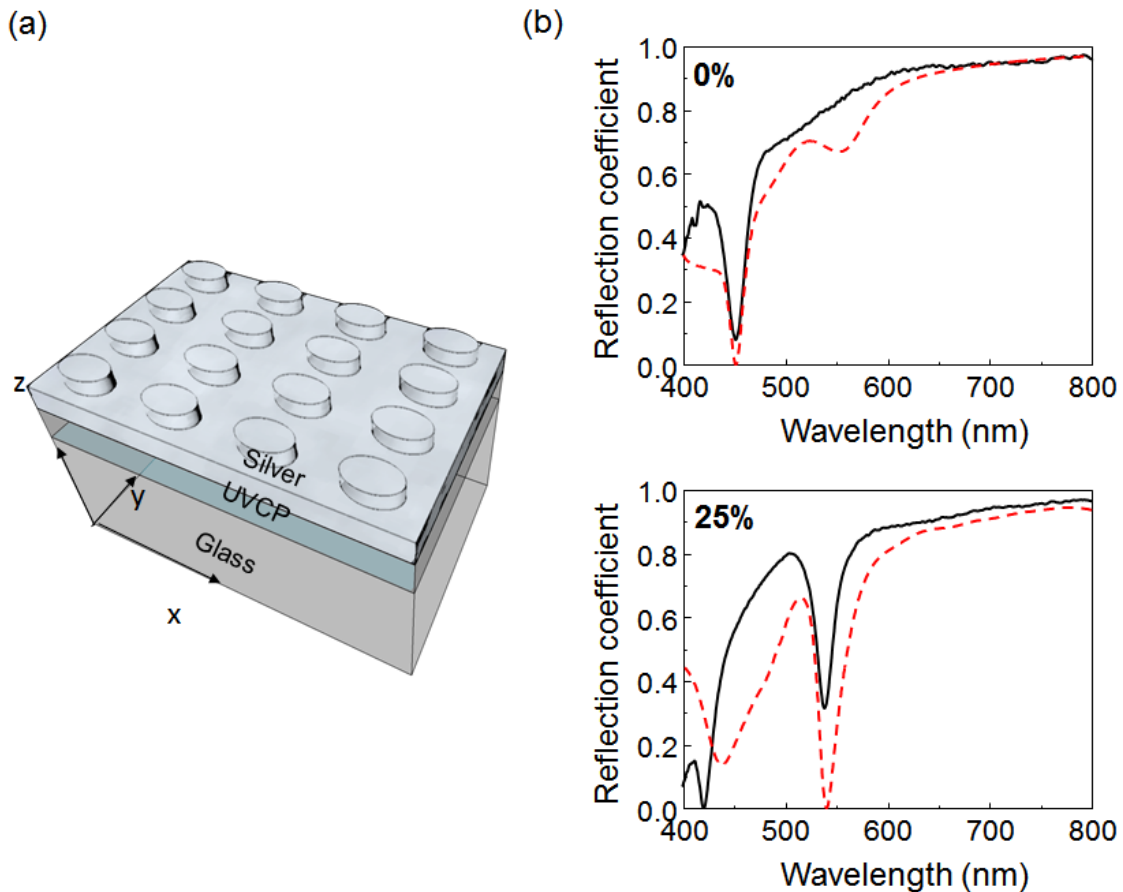


Figure 3-3. Optical characterization of 2D plasmonic crystals. (a) Schematic of a silver-coated plasmonic slab. (b) Simulations for 0% and 25% strain, compared to experimental data. The black solid lines represent the measurement results, and the red dashed lines represent the simulations.

The capability of programming the array lattice is particularly useful for some nanophotonic devices. As an example, we studied plasmonic crystals with different periodic arrays fabricated using the process described above. As a result of the different geometries,

these arrays exhibit distinct plasmonic resonances. The plasmonic crystal structure, shown in Figure 3-3(a), consists of a replicated 2D array of nanoposts with a 100 nm-thick silver coating, and supports grating-coupled surface plasmon resonance (SPR) modes. Excitation light that meets the resonance condition can be coupled into an SPR mode and may be strongly absorbed. As a result, the reflection spectrum exhibits a dip with the minimum reflectance at the SPR wavelength (λ_{SP}). The resonance wavelength can be estimated using the equation:

$$\lambda_{sp} = \sqrt{\frac{\epsilon_d \epsilon_m}{\epsilon_d + \epsilon_m}} \cdot \frac{\Lambda}{\sqrt{i^2 + j^2}} \quad 3-1$$

where Λ is the period of the grating, (i, j) represent the Bragg resonance orders, and ϵ_m and ϵ_d are the dielectric constants of metal and surrounding medium, respectively^{37,38}. Because the SPRs of plasmonic crystals are determined by the grating period shown in Equation 3-1, the programmable replica molding process can be used to finely tune the periodic array and obtain the desired SPR mode wavelength.

In fact, the resonance wavelength varies proportionally to the strain (ϵ) that is generated in the PDMS mold by the uniaxial stretch. In order to experimentally investigate the correlation between λ_{SP} and ϵ , we replicated 10 different arrays of nanoposts by placing the PDMS mold under a range of strains ($\epsilon = 0\%, 2.5\%, 5\%, 7.5\%, 10\%, 15\%, 20\%, 25\%, 30\%$, and 35%). The replicated 2D gratings were subsequently coated with a 100 nm-thick silver film to form the plasmonic crystals. The same PDMS mold was reused 10 times to produce the plasmonic devices. Reflection spectra of the plasmonic crystals were measured to identify their resonance wavelengths. Rigorous coupled wave analysis (RCWA) was used to simulate these reflection spectra. Details of the simulation and measurement are discussed in the experimental section. Figure 3-3(b) compares the measured and simulated reflection

spectra of devices fabricated with 0% and 25% strain. With 0% strain, the device exhibits a reflection dip at $\lambda_{SP} = 456$ nm; the x - and y -polarized SPR modes coincide in wavelength because the array structure is symmetric. As shown in Figure 3-4(a), the stretch applied during molding splits the differently polarized resonance modes. The SPR mode with the electric field polarized along the x -axis shifts to longer wavelengths with increased stretch; the shift is proportional to the degree of stretching. The corresponding compression along the y -axis causes the y -polarized SPR mode to move to shorter wavelengths. For $\epsilon = 35\%$, the plasmonic resonances are shifted by 111 nm and -41 nm for the x - and y - polarizations, respectively. Figure 3-4(b) summarizes λ_{SP} as a function of strain for both polarizations. The measured resonance wavelengths are fitted by straight lines with slopes of $\lambda_{SP}/\epsilon = 3.13$ and -1.14 nm/(% strain) for the x - and y -polarizations, respectively.

The array control in the nanoreplica molding method can also be used to examine and modify the photonic band diagram of photonic crystal slabs. In this study, the photonic crystal slab is based on a grating coupled waveguide, which is also known as a leaky-mode waveguide. The guided-mode resonance (GMR) phenomenon supported by this structure provides narrowband optical resonances³⁹⁻⁴¹. As shown in Figure 3-5(a), the photonic crystal slab consists of a replicated 2D grating on a glass substrate, which can couple light into and out of a thin-film dielectric waveguide coated on the surface of the grating. At a specific combination of wavelength and angle of incidence, the GMR mode can be excited with nearly 100% reflectance. Based on the diffraction grating equation, the GMR wavelength and the resonant angle can be calculated from the equations: Finally, n_1 , n_2 , and n_3 represent the refractive indices of the superstrate, the grating layer material, and the substrate,

respectively^{42,43}. Like plasmonic crystals, the resonance characteristics of a photonic crystal slab also depend on the array geometry.

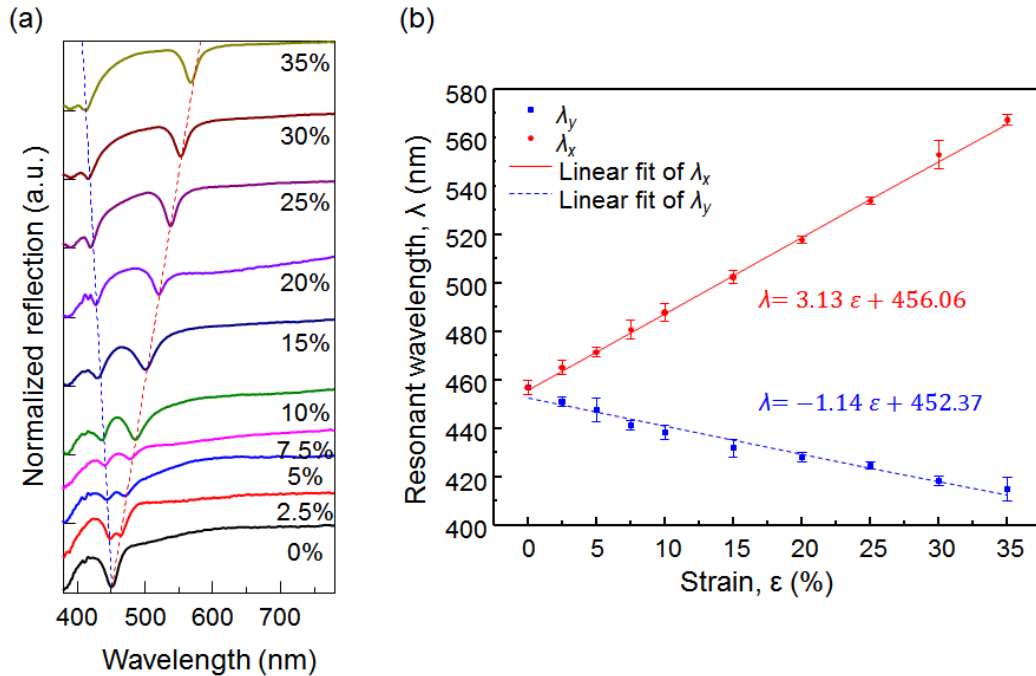


Figure 3-4. (a) The SPR reflection dips for plasmonic slabs fabricated with 0%, 2.5%, 5%, 7.5%, 10%, 15%, 20%, 25%, 30%, and 35% strain. The split between the dips for x- and y-polarizations follows the lattice period deviations in the x-direction (elongation) and y-direction (compression). (b) Plasmonic resonance wavelength with respect to applied strain. The SPR dips in the stretched and compressed directions from the experimental data in (a) are shown by the red dots and blue squares, respectively; linear fits to the resonance wavelengths, by the solid red and dashed blue lines. The error bars represent the standard deviation of 10 measurements taken at different locations on the sample.

Here, we demonstrate photonic crystal slabs with three different lattice arrangements, namely, the square, the rectangular, and the triangular lattice. The photonic crystal slabs were fabricated using the programmable replica molding approach, followed by coating with a 160 nm-thick TiO_2 layer (refractive index $n = 2.0$). The transmission spectra were measured using broadband light from the direction normal to the sample surface. As shown in Figure 3-5(b), the photonic crystal slab with a square lattice ($A_x = A_y = 300$ nm) shows two GMR modes at 560.2 nm and 591.6 nm, representing the TM-polarized and TE-polarized modes,

respectively. For the TM-polarized modes, the electric field components are perpendicular to the periodic modulation, while for the TE-polarized modes, they are parallel to the modulation. Because of the symmetry of the square lattice, the reflection measurement is independent of the excitation light polarization. Figure 3-5(b) also compares the measurement to the RCWA simulation. The discrepancy between measured and simulated resonance characteristics likely arises because the simulation does not take into account the slight divergence of the incident light.

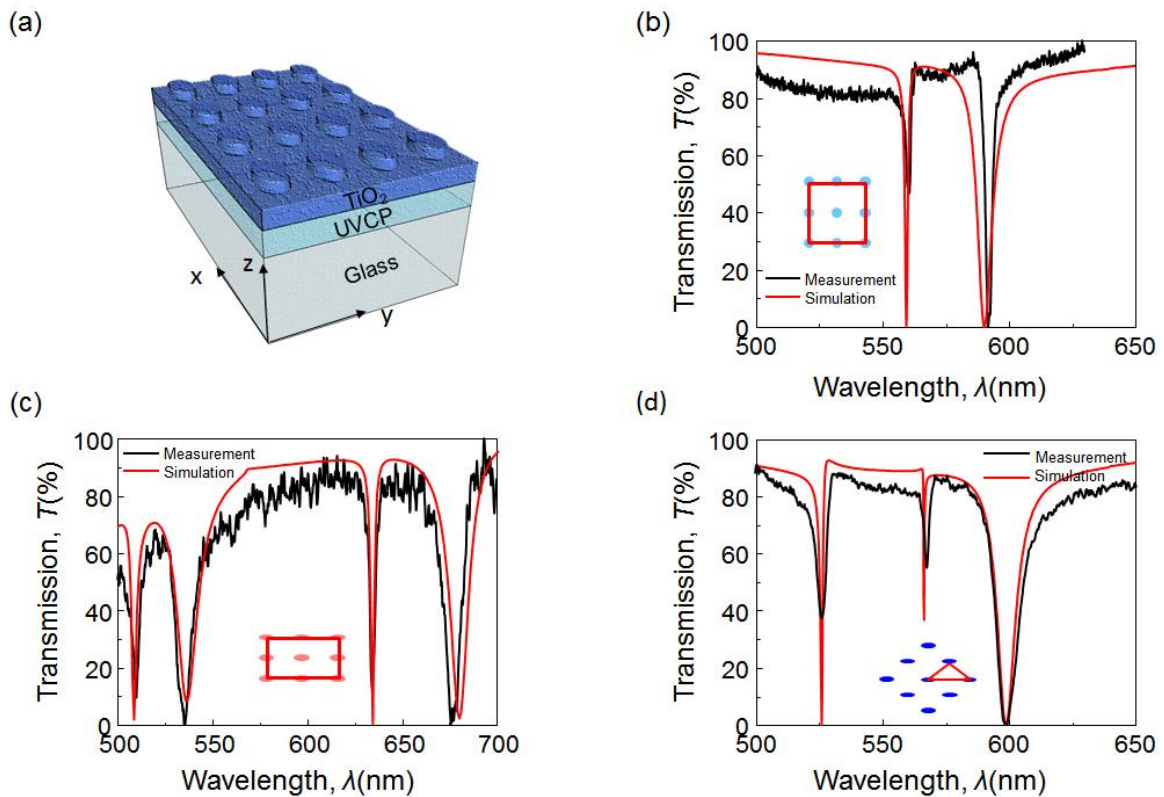


Figure 3-5. Reflection spectra of plasmonic crystals:(a) Schematic diagram of a photonic crystal slab with a rectangular lattice. Experimental and simulated transmission spectra of photonic crystal slabs when the resonance modes are excited from the normal direction, for a square (b), rectangular (c), and triangular lattice (d).

To generate a rectangular lattice, the PDMS mold was stretched with a uniaxial force along the x -axis to generate a strain of 25%. The replicated array structure shows two distinct

periods ($A_x = 375$ nm and $A_y = 280$ nm) along the x -axis and y -axis, respectively. As shown in Figure 3-5(c), the rectangular lattice slab exhibits two TM-polarized modes at 634.5 nm and 510.1 nm corresponding to the modified array periods. At the same time, there are also two TE-polarized modes locating at 677.2 nm and 535.5 nm. Next, to fabricate a photonic crystal slab with a triangular lattice (Figure 3-2(d)), the PDMS mold was stretched along its diagonal direction to achieve a strain of 35%. The measured transmission of the triangular lattice photonic crystal is shown in Figure 3-5(d). For comparison, the red curves in Figure 3-5(c) and (d) represent the transmission spectra calculated using an RCWA simulation.

To further investigate the effect of lattice arrangement, the dispersion of GMR modes as a function of incident angle was studied. Transmission spectra were recorded when the incident angle was scanned along the high-symmetry directions, as described in the experimental section. For the square lattice PC slab, the measured and simulated photonic band structures are shown in Figure 3-6(a). When the angle of incidence (θ_x) increases from the Γ point toward the X point, both TE-polarized and TM-polarized modes form three bands. The center “flat” band represents the GMR coupled with the excitation light through the grating modulation along the y -direction. In contrast, the GMR modes coupled through the grating modulation along the x -direction split into two bands, an upper band and a lower band with respect to their resonant wavelength. The lower TE-polarized band and upper TM-polarized band intersect at $\theta_x = 15^\circ$. When the angle of incidence changes along the Γ -M, the TE-polarized GMR modes form an upper band and a lower band. The TM-polarized modes branch into two upper bands and two lower bands.

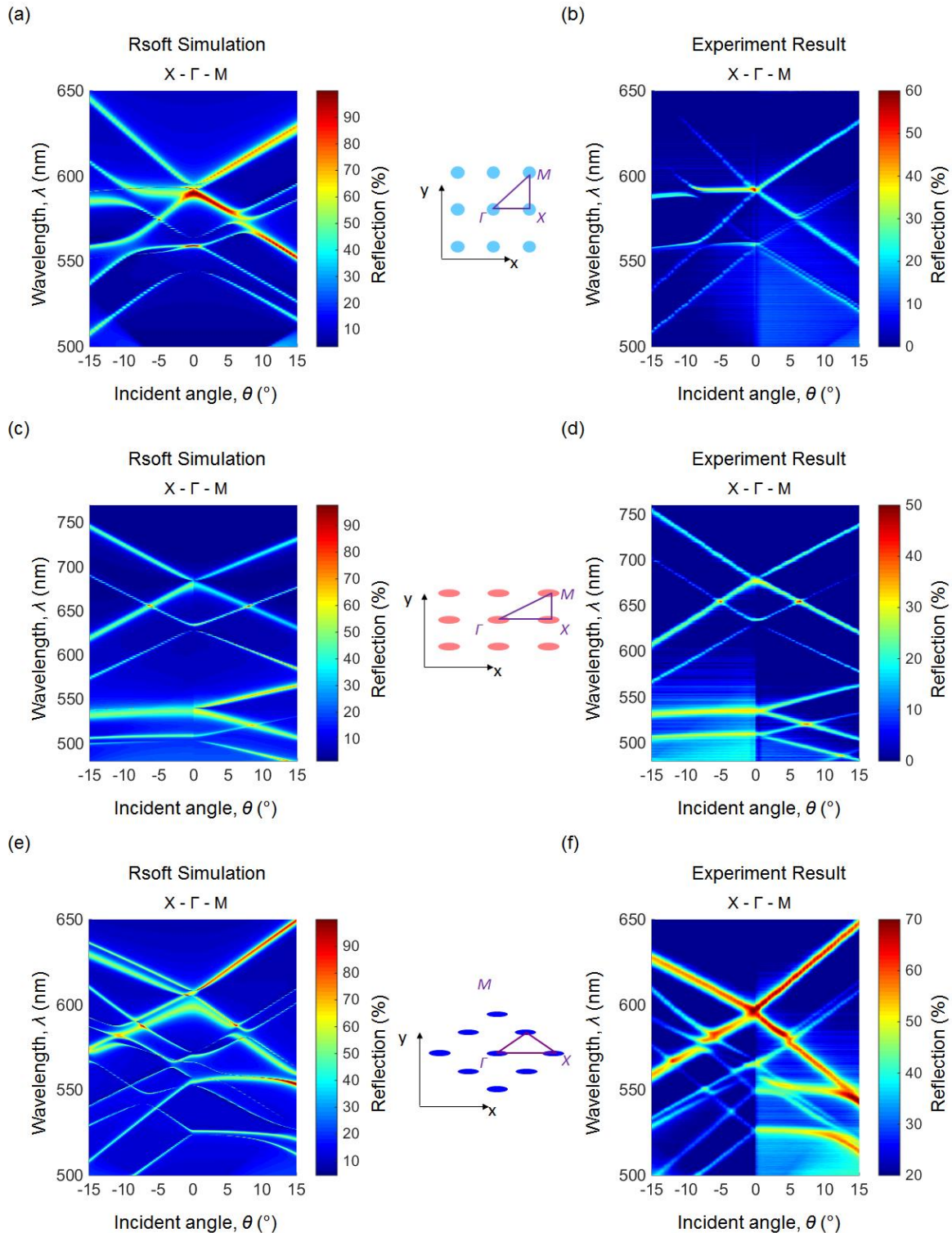


Figure 3-6. Photonic band diagrams derived from the transmission spectra. (a, b) Simulated and measured photonic band diagrams for the square lattice structure. (c, d) Simulated and measured photonic band diagrams for the rectangular lattice structure. (e, f) Simulated and measured photonic band diagrams for the triangular lattice structure.

Figure 3-6(b) shows the measured and simulated band structures for the rectangular photonic crystal slab with the angle of incidence scanned from the Γ point to the X and M points, respectively. When the angle of incidence increases from the Γ point towards the X point, two flat bands (one for a TE band and one for a TM) are observed. The flat bands are the GMR modes coupled *via* the grating modulation along the y -direction. The GMR modes coupled *via* the x -direction modulation are located in a longer wavelength region because the rectangular grating is not symmetric and Λ_x is larger than Λ_y . For both TE and TM polarizations, the GMR modes split into an upper band and a lower band. From the Γ point to the M point, all four GMR modes form two bands, resulting in eight different bands. Likewise, Figure 3-6(c) shows the experimental and calculated photonic band diagrams for the device with a triangular array, where the angle of incidence is scanned from the Γ point to the X and M points.

3.4 Conclusion

In summary, this paper reports a programmable nanoreplica molding method that facilitates fabrication of grating-based nanophotonic devices. Using a single PDMS mold, this fabrication method can produce sub-wavelength structures with various lattices. We adopted the stretchable PDMS mold, which was replicated from a glass stamp, to fabricate periodic nanostructures using UVCP material on a glass or a plastic substrate. During nanoreplica molding, the PDMS mold was stretched precisely to produce the desired lattice geometry. Nanophotonic devices, including plasmonic and photonic crystals, were formed by coating metal or dielectric thin films on the replicated UVCP. The optical resonances of these devices were characterized experimentally and compared to simulation results. For the plasmonic crystals, an SPR wavelength of 456 nm increased to 566 nm with application of 35% uniaxial strain during molding. The range of the resonance wavelengths could be even

greater with increased stretch, since the PDMS can endure as high as 100% strain^{44,45}. For the photonic crystal slabs, reflection filters with three different lattice geometries were fabricated. Rectangular and triangular lattices were successfully obtained from the original square lattice. The photonic band diagrams of all three devices were measured and showed good agreement with simulations.

3.5 Materials and Methods

Nanoreplica molding process: The master stamp with a 2D square array ($A = 300$ nm) of 150 nm diameter posts and an overall dimension of 50 mm \times 50 mm was fabricated using the glass thermal imprinting method with vitreous mold prepared by carbonization of replicated furan precursor[30, 31]. The glass master stamp was cleaned and treated using an anti-adhesion silane (Repel Silane, GE Healthcare) in order to facilitate the replications. The PDMS mold was fabricated from the master stamp by the thermally curing of a mixture of PDMS elastomer and curing agent (in a volume ratio of 1:10) on the master stamp. The thickness of PDMS molds was controlled to be 2 mm. After curing at 100°C for 4 hours, the solidified PDMS was peeled away from the master stamp. Then the PDMS mold was cut into a rectangle that has a length of 50 mm and a width of 15 mm. The orientation of the lattice on the PDMS mold was identified and marked. During the UV-based replica molding process, the PDMS mold was placed between two grips that were separated by $L \sim 45$ mm on a customized stage. One of the grips was fixed and the other one was pulled horizontally (along x -direction) by a linear translation stage. The translation stage induced strain values, $\epsilon_x = \Delta x/L$, where Δx is the amount of stretch. The PDMS mold was held at the desired length during the replica molding process. A layer of liquid UVCP (NOA 88, Norland Product Inc.) was squeezed between the PDMS mold and a glass coverslip. The UV-curing process took

place by exposing the coverslip/liquid UVCP/PDMS stack to UV illumination for 300 s. After curing, the replica of a 2D array of nanoposts and the PDMS mold were separated by peeling the coverslip away from the PDMS mold. The fully cured polymer preferentially adheres to the glass substrate without leaving any residue on the PDMS mold. Subsequent to the replica molding, a layer of dielectric (TiO_2) or silver thin film was deposited over the surface relief 2D grating by electron-beam evaporation to complete the device fabrication.

Reflection measurement for plasmonic crystals: Reflection spectra of plasmonic crystals were measured using a white light reflection setup. A halogen lamp was used as a broadband excitation source, and was coupled into a bifurcated fiber (BFY50HS02, Thorlabs), with a fiber tip collimator at the exit. An iris and a linear polarizer were placed in front of the collimator to control the spot size and polarization of the incident beam. The illumination assembly was attached to a kinematic mount for precise adjustment of the angle of incidence. The reflected light was coupled into a spectrometer (USB2000, OceanOptics) through the same bifurcated fiber. For measurement of its reflection spectrum, a plasmonic crystal sample was mounted on a motorized x - y translation stage and immersed in deionized water. A silver-coated mirror was used as the reference for reflectance. Software developed using C# was used to control movement of the translation stage and collect spectra from the spectrometer for chosen sampling locations on the plasmonic crystals. The measured spectra were fitted using a second-order polynomial function to find the resonance wavelength of the plasmonic modes.

Photonic crystal transmission and band diagram measurements: The dispersion band diagrams of the photonic crystal slabs were measured by recording the transmission spectra for multiple incident angles. The experimental setup for transmission measurement has three

main parts: a halogen lamp for white broadband illumination, a sample mount, and a spectrometer. The white light was collimated before exiting the coupling fiber. The light beam passed through the photonic crystal slab and the transmitted light was collected using a multimode fiber collector, which was connected to the spectrometer. The instruments were aligned horizontally and the plane of incidence was chosen to be the horizontal plane. The sample mount was carefully designed, with two perpendicular rotation stages and a kinematic mount, providing sufficient degrees of freedom for complicated and precise angle adjustments. At the beginning of each measurement, a sample was mounted with its top face perpendicular to the incoming light (at the Γ -Point). Then, based on the direction to be measured, i.e., Γ -X or Γ -M, the sample was rotated vertically so that the direction being measured was parallel with the horizontal plane. Next, the sample was rotated horizontally so that the incident angle θ was scanned accordingly from 0° to 15° by increments of 0.5° . For each θ the transmission spectrum was recorded, for both Γ -X and Γ -M directions, to form a data cube. The photonic band diagram was plotted using θ and λ as x -axis and y -axis, respectively.

Electromagnetic modeling: The RCWA simulations were performed to model the reflection and transmission spectra of the plasmonic crystals and photonic crystal slabs. The simulation region was setup to the unit volume of the periodic structures. Periodic boundary conditions were applied to truncate the calculation domain in x - y plane. Ten spatial harmonics were used at both x - and y -directions. For plasmonic crystals, the devices were illuminated from the direction normal to the surface by a plane wave. The incident wave was linearly polarized with the electric field oriented at 45° to x -axis in x - y plane. The material properties of silver were taken from the Palik's handbook, and then fitted by the multi-

coefficient model in the wavelength range from 300 nm to 1000 nm. Reflection spectra of plasmonic crystals were calculated in the wavelength range from 375 nm to 775 nm. The simulation of photonic crystal slabs generated their dispersion diagrams. The transmission spectra of a photonic crystal slab were recorded when the angle of incidence (θ) was scanned from 0° to 15° with an incremental of 0.5° . The dispersion diagrams for the Γ -X directions were shown by plotting the transmission spectra as a function of θ when $\varphi = 0^\circ$. The dispersion diagrams for the Γ -M directions were plotted when $\varphi = 45^\circ, 37.12^\circ, \text{ and } 90^\circ$, for the square, the rectangular, and the triangular lattices, respectively.

3.6 Acknowledgements

The research was supported by the startup fund of Iowa State University, 3M Non-Tenured Faculty Award, and the Basic Science Research Program through the National Research Foundation of Korea (NRF) funded by the Ministry of Science, ICT & Future Planning (NRF-2013R1A2A2A01068561). J. L. acknowledges support from the National Science Foundation through grant CMMI-1363468. L. D. acknowledges support from the National Science Foundation through grant ECCS-0954765.

CHAPTER 4. LINEAR VARIABLE PHOTONIC FILTERS

4.1 Abstract

This paper presents the fabrication methodology of a linear variable photonic crystal (PC) filter with narrowband reflection that varies over a broad spectral range along the length of the filter. The key component of the linear variable PC filter is a polymer surface-relief grating whose period changes linearly as a function of its position on the filter. The grating is fabricated using a nanoreplica molding process with a wedge-shaped elastomer mold. The top surface of the mold carries the grating pattern and the wedge is formed by a shallow angle between the top and bottom surfaces of the mold. During the replica molding process, a uniaxial force is applied to stretch the mold, resulting in a nearly linearly varying grating period. The period of the grating is determined using the magnitude of the force and the local thickness of the mold. The grating period of the fabricated device spans a range of 421.8–463.3 nm over a distance of 20 mm. A high refractive index dielectric film is deposited on the graded-period grating to act as the waveguide layer of the PC device. The resonance reflection feature of the device varies linearly in a range of 680.2–737.0 nm over the length of the grating.

4.2 Introduction

Variable optical filters are designed to exhibit graded transmittance or reflectance depending on the location, where the measurement is performed on the filter^{46–48}. Among the many types of variable filters, the linear variable bandpass filter, with a peak transmission wavelength varying linearly in one direction and remaining uniform in the other direction, is most popular. This type of optical filter is desirable for several applications, including in a compact spectrum analyzer, where the filter is directly attached to a charge-coupled device

(CCD) sensor, and for use as a color filter in hyperspectral imaging^{49,50}. The linear variable effect can be achieved by using a Fabry–Perot cavity with a linearly graded cavity length. While Fabry–Perot interference filters are used for such purposes, other methods may offer a lower cost, a narrower bandwidth, and an improved wavelength range. One-dimensional photonic crystals (PC), with a grating-coupled waveguide, which support guided-mode resonance (GMR), have demonstrated the extraordinary ability of generating narrowband reflections at specific wavelengths^{39,51,52}. Dobbs *et al.*¹² reported a PC-based linear variable filter that uses a grating structure in conjunction with a waveguide layer whose thickness progressively changes. PC-based devices have also been found to be useful for a variety of other applications, including spectrum analysis, optical biosensors, optical communications, and displays^{40,53,54}. The optical characteristics of a PC filter, such as the resonance wavelength, peak reflection efficiency, and linewidth, can be engineered by controlling the geometrical parameters of the device and its component materials^{42,55}. Currently, the application of the PC devices is mainly challenged by the demanding of fabrication processes to produce gratings on a sub-micrometer scale. Conventional lithography methods, such as electron beam lithography and deep UV lithography, are expensive with limited throughput. Recently, techniques, such as interference lithography and soft lithography, have been successfully applied for the fabrication of PC devices^{5,56}. In particular, nanoreplica molding, as a soft lithography process, allows inexpensive fabrication of nanoscale gratings by transferring the pattern of a mold to a target substrate using photocurable or thermally curable polymer materials¹⁰.

In this work, we present a PC filter that exhibits a spatially variable resonant reflection along the length of the filter. The device is fabricated using nanoreplica molding

with a wedge-shaped polydimethylsiloxane (PDMS) mold. During the nanoreplica molding process, the elastic PDMS mold is deliberately stretched to generate surface-relief gratings with a linearly graded period along the length of the device. When the elastic mold is elongated by 22.3%, the grating period spans a range of approximately 421.8–463.3 nm across the 20-mm length. Following replica molding, the gratings are coated with a 160-nm-thick titanium dioxide (TiO_2) dielectric film, which functions as the light-confinement layer of the PC filter. The PC filter is then characterized via optical reflection to show the graded resonant reflection in the wavelength range of 680.2–737.0 nm with a gradient of 2.85 nm/mm.

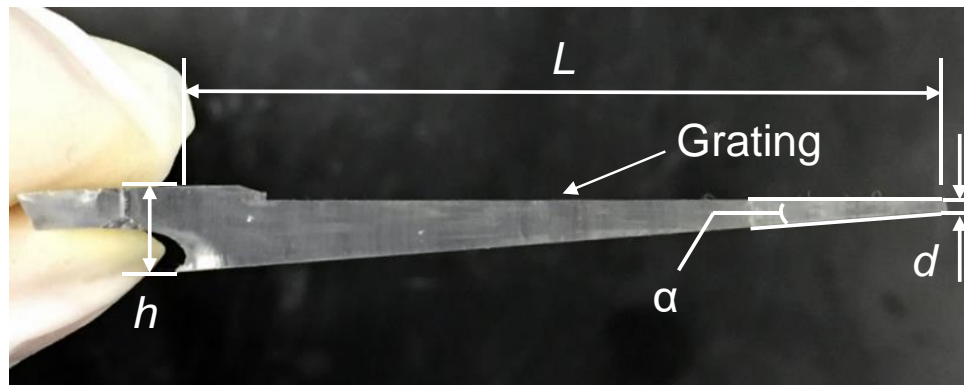
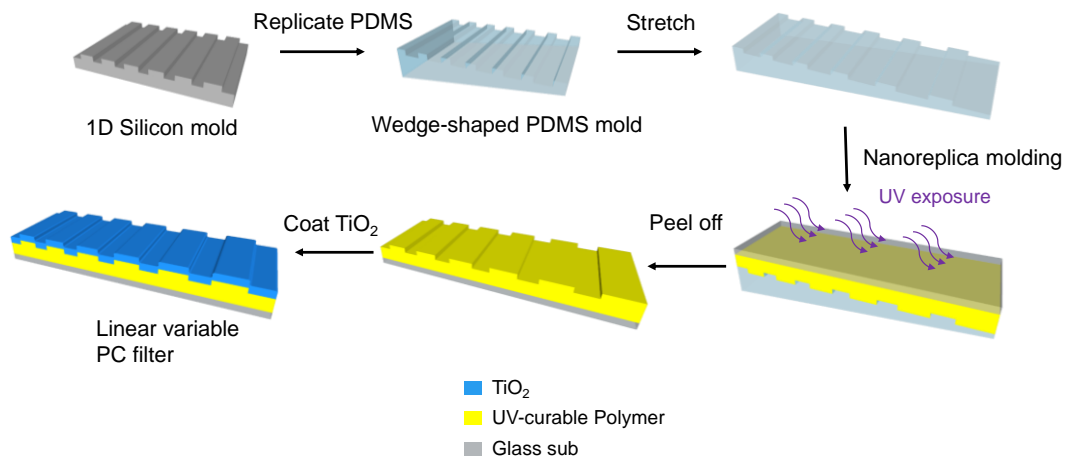


Figure 4-1. (a) Schematic of the linear variable replica molding process. (b) A photo showing the dimensions of the replicated wedge-shaped PDMS.

4.3 Methodology

The proposed replica molding process for the fabrication of linear variable PC filters is summarized in Figure 4-1(a). The key steps of the process include mold preparation, mold stretching, pattern transfer, and mold release. The first step is the preparation of the PDMS mold of the desired grating pattern, with a negative surface profile and linearly increasing thickness. The PDMS mold used to fabricate the PC device was cast from a silicon master wafer bearing a uniform grating pattern with a period, depth, and duty cycle of 360 nm, 60 nm, and 40%, respectively. The grating on the silicon master wafer was fabricated using deep UV photolithography and reactive ion etching. To obtain the PDMS mold, the silicon master wafer was placed in a petri dish with 15 g of uncured PDMS (Sylgard 184). In order to ensure the PDMS mold was tapered, a 30-mm-thick acrylic block, which was tilted at an angle to the top surface of the silicon master wafer, was used to form the uncured PDMS into a wedge shape as shown in Figure 3.2-S1[20a]. The inclination angle α was carefully controlled to generate the desired wedge shape for the PDMS mold. The PDMS wedge was thermally cured (70 °C, 4 h) and then slowly separated from the silicon master and the acrylic bar. Figure 4-1(b) shows the fabricated PDMS wedge with an inclination angle, base height, rise, and length of $\alpha = 4.8^\circ$, $h = 4.1$ mm, $d = 1$ mm, and $L = 36.7$ mm, respectively. The tapered ends of the PDMS mold were aligned parallel to the grating (Figure 4-1(a)). Subsequently, the elastic PDMS mold was stretched to produce a surface with a linearly graded period. As shown in Figure 4-1(a), a uniaxial force was applied to the PDMS mold perpendicular to the grating direction. As a result, the one-dimensional grating structure was stretched and its period increased depending on its position along the PDMS wedge. The local strain can be represented by

$$\varepsilon(x) = \frac{F}{wt(x)E_{PDMS}} \quad 4-1$$

where F is the applied force, E_{PDMS} is the Young's Modulus of the cured PDMS, x is the position on the mold along the stretched direction, and w and $t(x)$ are the width and the thickness of the mold, respectively. As shown in Figure 4-1(b), the thickness of the mold can be represented with the linear expression

$$t(x) = h + (L - x)\tan(\alpha) \quad 4-2$$

The local strain $\varepsilon(x)$ is large where the PDMS mold is thin, and vice versa. Consequently, the elongation of the grating is a function of the position along the PDMS mold, where the period of the stretched grating is

$$\Lambda(x) = \Lambda_0 \varepsilon(x) = \Lambda_0 \frac{F}{w\{h+(L-x)\tan(\alpha)\}E_{PDMS}} \quad 4-3$$

where Λ_0 is the unstretched grating period. The grating pattern on the stretched PDMS mold was replicated onto a glass substrate using the nanoreplica molding process. Briefly, a layer of liquid UV-curable polymer (Norland Optical Adhesive 88) was squeezed between the stretched PDMS mold and a glass substrate. The liquid polymer was then cured by exposing to UV light (Spectroline Spectrolinker XL-1500) with a dose of 120 mJ/cm². Once exposed to UV light, the UV-curable polymer was solidified and subsequently released from the PDMS mold. Because the PDMS surface is hydrophobic without any special surface treatment, the cured polymer layer preferentially sticks to the glass substrate. Following replica molding, a dielectric thin film was deposited over the replicated polymer grating as the waveguide layer for the PC structure. In this example, a 160-nm-thick film of TiO₂ (refractive index = 2.1) was deposited using an electron beam evaporator.

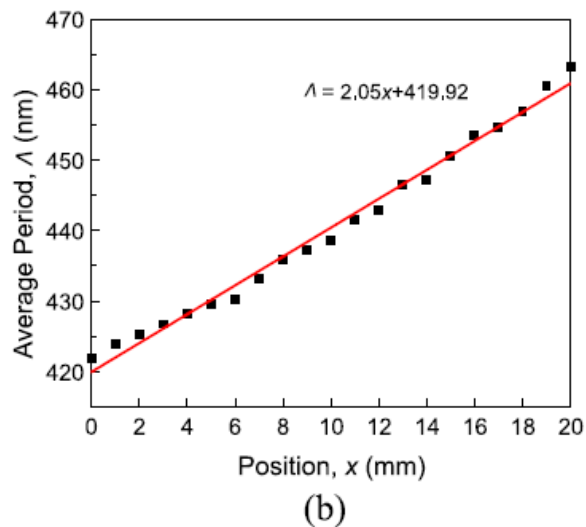
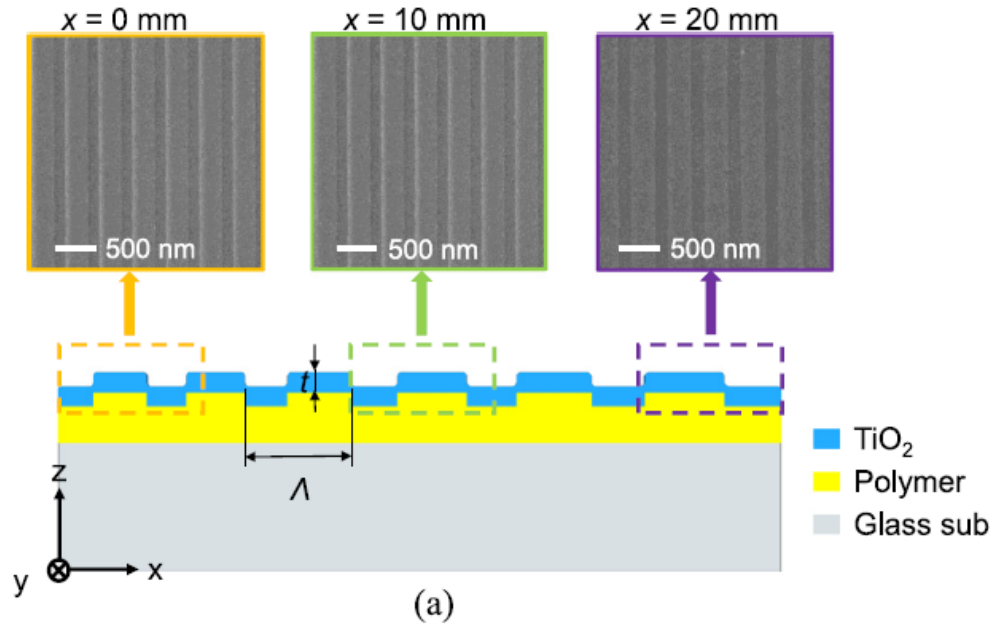


Figure 4-2. (a) Schematic cross section of the PC filter structure (not to scale) and the SEM images of the replicated grating at three different positions on the sample. The labeled x values represent the locations of the measurements along the gradient direction of the PC filter sample. The grating periods of the left panel, center panel, and right panels are $\Lambda = 421.8$ nm, $\Lambda = 438.7$ nm, and $\Lambda = 463.3$ nm, respectively. (b) Measured grating periods as a function of lateral position on the fabricated PC filter. The periods were at positions between $x = 0$ mm and $x = 20$ mm with increment of 1 mm. The coefficient of determination, R^2 for the linear fitting (red line) is 0.989.

A schematic cross-sectional diagram of the linear variable PC device is shown in

Figure 4-2(a). On a macroscopic scale, the grating period Λ is non-uniform and dependent on

its location along the length of the PC filter. In this work, the PC device was fabricated when the PDMS mold was stretched to 122.3% of its original length. Scanning electron microscopy (SEM) images in Figure 4-2(a) were taken at three locations along the sample, corresponding to the far left ($x = 0$ mm), center ($x = 10$ mm), and the far right spot ($x = 20$ mm). Using the SEM images, the period was calculated as an average across eight ridge/groove pairs with ImageJ. The measured value of the periods from the SEM images was $\Lambda = 421.8$ nm ($x = 0$ mm), $\Lambda = 438.7$ nm ($x = 10$ mm), and $\Lambda = 463.3$ nm ($x = 20$ mm). To further investigate the relationship between the grating period and the position, the grating period was measured using the SEM images (Figure 3.2-S2 in the supplemental material) at 20 different locations ranging from $x = 0$ to $x = 20$ mm with an increment of 1 mm. The measured grating periods as a function of lengthwise location are summarized in Figure 4-2(b). In an effort to study the linearity of the relationship, the data was fitted with a linear function, as illustrated in Figure 4-2(b). The coefficient of determination is $R^2 = 0.989$ for the fit, suggesting a nearly linear dependency of the period on the location along the length of the PC device. We also confirmed the morphology of the fabricated device using an atomic force microscope (AFM). The AFM images in Figure 3.2-S3 show the grating depth decreases from 60 nm to about 25 nm due to the stretch-induced compression along the surface normal of the grating. Later on, the change of grating depth can be taken into account during the design of the grating pattern of the silicon master wafer.

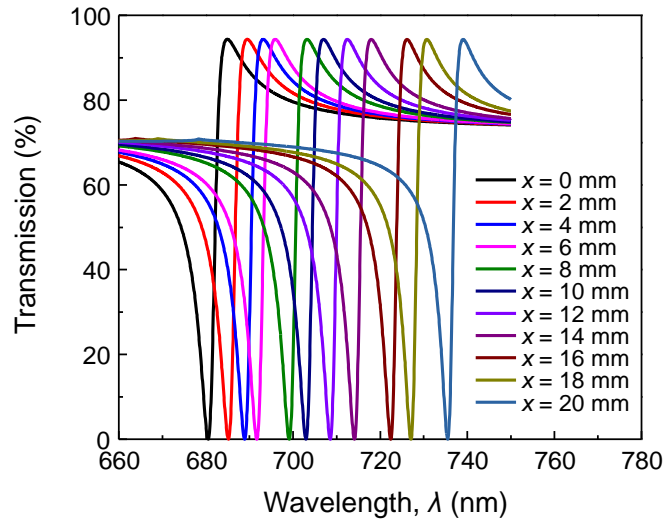
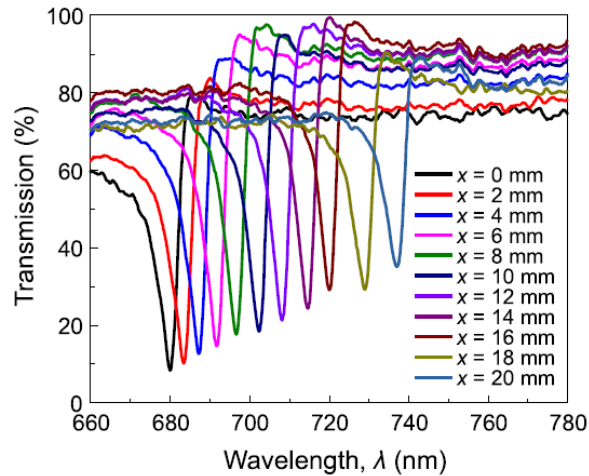


Figure 4-3. Calculated transmission spectra obtained by the RCWA simulation for the graded PC filter at 11 locations spanning 20 mm with increments of 2 mm.

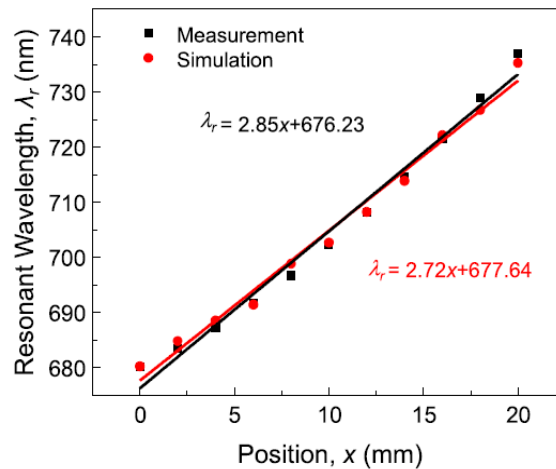
4.4 Results and Discussions

For identifying the optical resonances of the graded PC filter, numerical simulations of the replicated polymer grating coated with a 160-nm-thick TiO_2 film were performed. The periodic PC structure was modeled using rigorous coupled wave analysis (RCWA). Since the PC structure is polarization dependent, the numerical model used a linearly polarized incident light with the electric field parallel to the grating lines to excite the transverse electric (TE) modes. The incident beam was normal to the PC surface. The refractive indices of the polymer grating and TiO_2 film were 1.47 and 2.2, respectively. The grating depth was 25 nm. The grating periods used in the RCWA simulation were obtained from the measurement results shown in Figure 4-2(b). Figure 4-3 shows the calculated transmission spectra at 11 different positions spanning a distance of 20 mm along the sample with increments of 2 mm. As expected, the wavelength of the transmission dip increases with increasing grating period. The resonance wavelength, which is referred to as the wavelength

at the minimal transmittance, varies from 680.3 nm to 735.3 nm with a full-width half-maximum (FWHM) of approximately 7 nm.



(a)



(b)

Figure 4-4. (a) Measured transmission spectra with TE polarization at the 11 locations specified in the numerical study. (b) Dependence of measured and calculated resonant wavelengths on the lateral position. The resonant wavelengths are fitted by the solid lines, which show a high degree of linearity with coefficient of determination, R^2 of 0.983 and 0.986, respectively.

To experimentally characterize the optical resonances of the graded PC filter, transmission spectra of the fabricated device were measured at the positions mentioned in the above numerical study. The measurement setup used a halogen lamp as the excitation source,

which was coupled to a multimode fiber with a fiber tip collimator. An iris and a linear polarizer were placed in front of the collimator to control the spot size and polarization of the incident beam, respectively. The transmitted light was collected by another fiber and recorded by a spectrometer (USB2000, OceanOptics). The PC device was mounted on a motorized stage that translated the device along the gradient direction of the grating period. The orientation of the device was adjusted to the normal-incidence condition. Figure 4-4(a) shows the measured transmission spectra with TE polarization at 11 locations from $x = 0$ mm to $x = 20$ mm. At $x = 0$ mm, the resonance wavelength is 680 nm, and the resonance gradually shifts to 737 nm at $x = 20$ mm. This result clearly demonstrates that the spectral position of the optical resonance is directly related to the location of measurement for the PC device.

Figure 4-4(b) shows the dependence of resonance wavelength on the lateral position along the gradient direction of the grating period. The measured spectra are each fitted using a second-order polynomial function to determine the resonance wavelengths. For comparison, the result of the numerical simulation is plotted in red. The total shift of the resonance wavelength is 57 nm over a distance of 20 mm, resulting in a gradient of 2.85 nm/mm. The data points were fitted with a linear curve to demonstrate the dependence of the resonance wavelength on the location of measurement for the PC filter. According to the coefficients of determination, the relationship is linear, owing to the nearly linear change of the grating period and the linear relationship between grating period and resonance wavelength within the wavelength range of this study. In addition, Figure 4-3 and Figure 4-4 show good agreement between the simulation and experimental results.

The spectral bandwidth is one of the performance metrics of linear variable filters. Two factors determine the bandwidth of a graded PC structure. The first factor is the linewidth of the guide-mode resonance, and the second is the spatial gradient of the resonance. We studied the dependence of the bandwidth on the spot size of the light beam in order to clarify the effect of each factor. An iris was placed in front of the PC device to control the beam spot size. Figure 4-5 shows the normalized transmission spectra measured at the center of the filter ($x = 10$ mm) with spot sizes of 1 mm, 2 mm, 3 mm, and 4 mm. When the beam spot size decreases from 4 mm to 2 mm, the FWHM reduces from 10.4 nm to 7.8 nm. Future reduction of the spot size from 2 mm to 1 mm reduces the FWHM from 7.8 nm to only 6.5 nm. With a beam spot size of 1 mm, the measured bandwidth is close to that of the RCWA simulation, which ignores the variation of the grating period. Therefore, when the beam size is as small as 1 mm, the bandwidth is limited by the resonance linewidth, rather than the gradient effect. The bandwidth of the fabricated variable filter is comparable to the commercial products. For example, the FWHM of the linear variable VIS to NIR bandpass filter (LVVISNIRBP, Delta Optical Thin Film) is approximately 10 nm in the same wavelength range.

4.5 Conclusions

In summary, a new approach was developed to fabricate a PC device with a linear variable resonance along its length. The fabrication approach is based on the nanoreplica molding process and uses a stretchable PDMS wedge as the mold. During the molding process, stress is applied to the PDMS mold, generating elongations as a function of the specific location on the wedge-shaped mold. The elongation of the grating on the mold surface is determined by the local thickness of the mold, the applied stress, and the Young's modulus of the PDMS. The period of the replicated polymer grating spans a range of 421.8–

463.3 nm over a distance of 20 mm. The results of the optical characterization show that the resonance wavelength of the PC filter varies across a spectral range of 57 nm with a gradient of 2.85 nm/mm. The linear variable PC device has a number of potential applications. In particular, the narrow bandwidth feature of the GMR mode is desirable for spectral analysis and can be utilized to build a miniaturized spectrometer⁵⁷. The performance of the PC filter will be further improved by implementing the three-layer PC structure to obtain a transmission resonance and a reduced linewidth of the resonance⁵⁸.

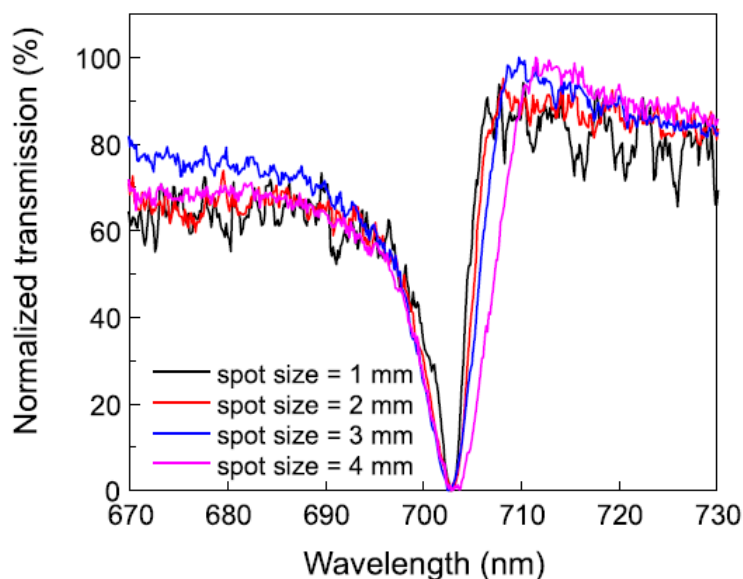


Figure 4-5. Measured transmission resonance at $x = 10$ mm with spot sizes 1 mm, 2 mm, 3 mm, and 4 mm. The FWHM of the resonances are 6.5 nm, 7.8 nm, 8.4 nm, and 10.4 nm, respectively.

4.6 Acknowledgements

ML acknowledges support by start-up funding from Iowa State University and the 3M Non-Tenured Faculty Award. JL acknowledges support from the National Science Foundation through grant CMMI 1363468. ACH acknowledges support from the National Science Foundation through grant CHE 1213582.

CHAPTER 5. PHASE-CHANGE MATERIAL FILM INCORPORATED GMR FILTER

5.1 Abstract

This paper reports a tunable photonic device that incorporates a nanometer-thin layer of phase-change material, $\text{Ge}_2\text{Sb}_2\text{Te}_5$ (GST), in a photonic crystal (PC) structure. The PC structure is based on a one-dimensional grating waveguide with a metal cladding on one side of the zinc sulfide waveguide. The metal-cladding PC structure supports the guided-mode resonance (GMR) mode that selectively absorbs light at a particular wavelength. Inserting the GST material into the waveguide makes it possible to control the GMR mode. Here, the GST-PC device were numerically designed and optimized to obtain a significant tuning around 1550 nm. The tuning effects were experimentally demonstrated by the crystallization or re-amorphization of the GST thin film. A spectral shift of the GMR mode resonant wavelength from 1440 nm to 1620nm has been achieved for the crystallization process. The phase tuning of GST exhibits good repeatability as demonstrated by switching the GMR mode between amorphous and crystalline phases of GST for multiple cycles. The GST-PC device represents a new approach for tuning optical resonances in the NIR.

5.2 Introduction

Photonic crystal (PC) devices are known to support the guided-mode resonance (GMR)^{39,55}. A typical PC device can be seen as a combination of a substrate, a sub-wavelength grating coupler and a high refractive index dielectric waveguide. The parameters for the GMR modes that supported by the PC devices are determined by the external light stimulation, the geometry of the grating coupler, and the materials of each component. For example, the resonant wavelength of the GMR modes can be predicted using the periodicity of the grating and the refractive indices of the waveguide and the cladding materials^{42,59}.

Because of the high peak reflection efficiency and the high sensitivity to environment refractive index of GMR modes, PC devices have been widely utilized in many fields, such as optical communications, displays, lasers, photovoltaics and biosensors^{6,33,40,60–66}.

One main application for the PC devices are optical filters or optical switches, where a big challenge for PC devices is to control their optical response precisely to meet specific applications. In many cases, a wide range of continuously tunable resonant wavelengths provided by a single device is highly desirable. To address such problem, researchers has developed various approaches. One approach is to introduce varying geometries in the PC device structure, where the periodicity or waveguide thickness are modulated over the device surface^{11,12}. Another approach is incorporating tunable materials, such as liquid crystal to change local refractive index, so that the spectral signature of GMR modes can be modulated^{13,14}. For example, liquid crystal has been used to tune the GMR modes but the tuning requires a few milliseconds due to the slow alignment of liquid crystal molecules.⁵

Phase-change materials, such as Germanium Antimony Telluride, are famous for the high contrast of their electrical and optical properties upon switching between amorphous and crystalline states.^{17,19} Among them, $\text{Ge}_2\text{Sb}_2\text{Te}_5$ (GST) is a main type that originally known for its application in rewritable CD-RW discs.⁶⁷ Nowadays, GST are still attracting tons of attention for its important role in non-volatile phase-change memories (NVPCM),^{68,69} as well as nanophotonic devices.^{70–74} GST is an desirable active optical material in the near-infrared, for its large refractive index contrast between crystalline and amorphous phases, a relatively low extinction coefficient (compared to that in the visible spectrum), rapid transition (< 30 ns), and good stability in room temperature,^{19,68} and the conditions for the phase transitions to occur is not difficult to meet.⁷¹

This paper reports a tunable A GST-incorporated PC device (GST-PC) with a periodicity of 1000 nm was fabricated and optically characterized. GMR modes of the GST-PC were numerically studied to optimize GST position and thickness. The crystallization and re-amorphization of the GST thin film inside GST-PC were realized using heating and line-focused pulse laser scanning, respectively. The refractive indices for a GST-PC device with as-deposited GST, crystallized GST and melt-quenched GST were measured by ellipsometry. And the corresponding optical responses were studied using a reflection setup. A large resonant wavelength shift for crystallization process from 1440 nm to 1620nm was observed. Finally, the device was switched between amorphous and crystalline phases of GST for multiple cycles as a demonstration of repeatability and reliability. A 45-nm clearance was achieved using this tuning technique.

5.3 Results and Discussion

5.3.1 Structure of GST-incorporated photonic crystal filter

Figure 5-1(a) shows the schematics of the tunable PC filter that incorporates a GST thin film. The tunable filter consists of a stack of thin films on a one-dimensional (1D) surface relief grating. The thin-film stack includes a gold cladding layer, a zinc sulfide (ZnS) waveguide layer, and a GST thin film embedded in the ZnS layer. The 1D sinusoidal grating was fabricated on a glass substrate using a spin-on-glass (SOG) and nanoimprint process.⁷⁵ The simple nanoimprint process enables us to create sub-waveguide gratings in SOG inexpensively. Following the fabrication of the SOG grating, the gold, ZnS, and GST films were deposited on the grating surface using physical vapor depositions. Details of the device fabrication process are described in the experimental section with the process flow illustrated in Figure S1. Figure 5-1(b) is a photograph of the fabricated device over an area of 18×15

mm². Scanning electron microscopy (SEM) images in Figure 5-1(c) and (d) show the top-view surface profile and cross-sectional structure.

The ZnS film has a high refractive index ($n_{\text{ZnS}} = 2.29$ at 1550 nm) and functions as the waveguide layer to confine light along the z -axis. The gold film ($t_{\text{Au}} = 80$ nm) locates below the ZnS layer serves as the metal cladding of the ZnS waveguide. The grating structure can couple the incident light into a GMR mode supported by the ZnS grating waveguide.³⁹ At the resonant wavelength (λ_r), the light is strongly absorbed owing to the loss of the gold cladding. On the other hand, the gold layer effectively reflects light that does not meet the resonant condition. As a result, the metal-cladding PC supports the GMR modes that exhibit reflection minimums or dips in the reflection spectrum.

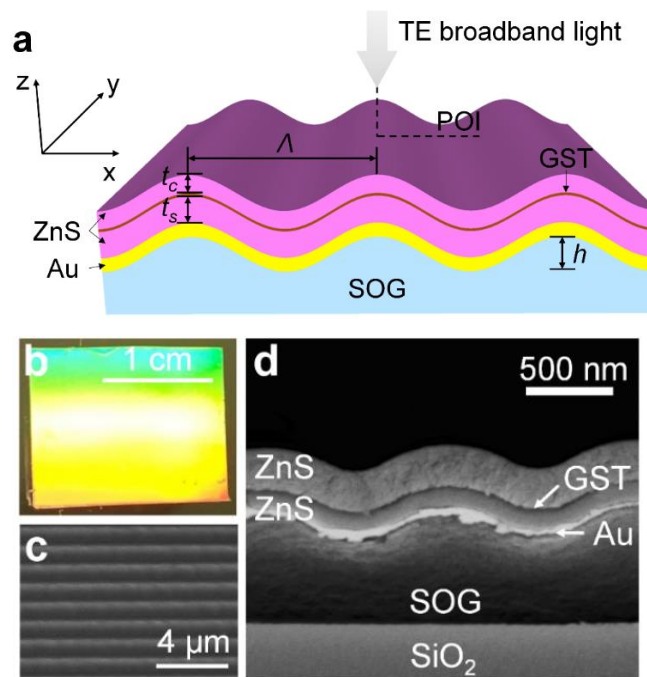


Figure 5-1. Grating waveguide structure with GST film. (a) Schematic diagram of the GST-PC device consisting of a sinusoidal grating and a stack of thin films. The grating is fabricated using on glass with period of Λ and depth of h . The stack including the Au, ZnS, GST, and ZnS layers are coated on the SOG grating. The thicknesses of the Au, ZnS, and GST films are t_s , t_c , and t_{GST} , respectively. (b) A photograph of the fabricated device. The overall size of the device is 18×16 mm². (c) Top view SEM image and (d) cross-sectional view SEM image showing the thin-film stack on the SOG grating.

To tune the spectral signature of the GMR mode, a thin film of GST is integrated into the ZnS grating waveguide. The thickness of GST and its position in the ZnS waveguide are optimized to maximize the effect of the phase transition on the change of GMR modes. By inducing phase transitions between crystalline and amorphous states for GST, the effective refractive index for the waveguide can be modulated by the change of refractive index and loss of the thin GST film, and thus, shifts GMR modes in the reflection spectrum.

5.3.2. Tuning of optical resonances of the metal-cladding

Rigorous coupled wave analysis (RCWA) was used to facilitate the design of the tunable GMR device. Optical characteristics, including reflection spectra and near field distributions, were calculated with the GST film in the amorphous and crystalline states. The device is designed to operate in the near IR telecom window (around 1550 nm), where the GST has relatively small material loss and large change in refractive index during phase transition. The refractive index of the GST film was measured using a spectroscopic ellipsometer (VASE, J. A. Wollam) and shown in Figure S2. The 1D sinusoidal grating has a period and depth of 1 μm and 150 nm, respectively. In the RCWA simulation, the device is illuminated with a normally incident unit magnitude plane wave propagating along the $-z$ -axis with an electric field polarization along the grating direction (y-axis) (Figure 5-1(a)), which can be coupled into transverse electric (TE) GMR modes.

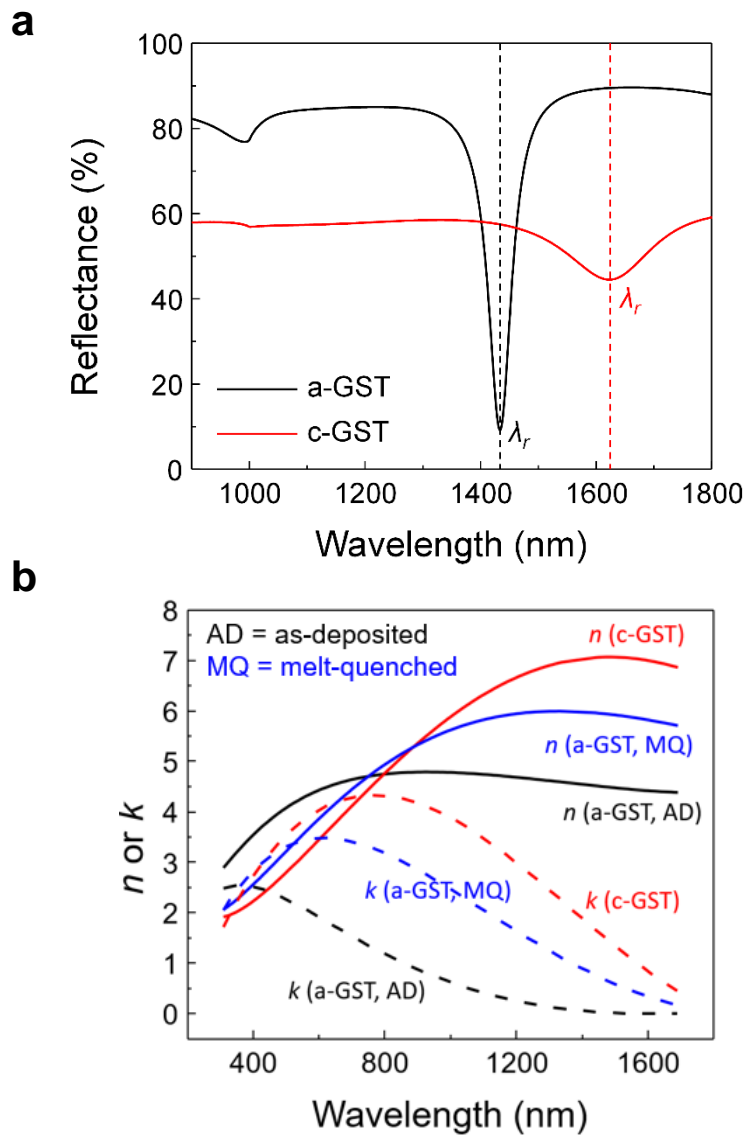


Figure 5-2. Calculated reflection spectra for GST-PC. (a) Simulation results of the reflection spectra for GST-PC devices integrated with GST thin film in amorphous (black) and crystalline (red) states. The resonant wavelength shift, $\Delta\lambda_r$, was defined as the change of the resonant wavelength. (b) Measured refractive indices (n , solid lines) and extinction coefficients (k , dashed lines) in the near infrared wavelength range: n (solid lines) and k (dash lines) for the as-deposited amorphous GST (black), crystalline GST (c-GST, red), and melt-quenched amorphous GST (a-GST, royal blue).

To investigate the change of GMR mode owing to the phase transition of GST, device designs with different GST thickness (t_{GST}) and position (d_{GST}) in the ZnS waveguide were modelled. We first set $t_{\text{GST}} = 8.5$ nm and the ZnS thickness of $t_{\text{ZnS}} = 200$ nm. The position of

the d_{GST} denotes the distance of GST film from the gold cladding. The value of d_{GST} was increased from 0 to 200 nm. The GST film locates on top of the gold cladding and the ZnS waveguide when $d_{\text{GST}} = 0$ and $d_{\text{GST}} = 200$ nm, respectively. For $d_{\text{GST}} = 200$ nm, the calculated reflection spectra for a-GST and c-GST are shown in Figure 5-2(a). The dips in the reflection spectra represent the absorption resonance of a metal-cladding GMR mode. The amount of resonant wavelength shift ($\Delta\lambda_r$) is defined as the change of minimal reflection wavelength when the GST film transits from the amorphous to crystal state. It can be seen that the resonant wavelength shift is nearly zero when $d_{\text{GST}} = 0$ (red circle in Figure 5-2(b)). Since the tangential electric field (E_y) diminishes at metal surface as shown in the left panel of Figure 5-2(c), the GMR mode is insensitive to the phase transition. Moving the GST film away from the metal cladding increases the resonance wavelength shift until the shift reaches its maximum near $d_{\text{GST}} = 135$ nm (yellow star in Figure 5-2(b)). The phase transition process results in the resonance wavelength shift over 200 nm. After the maximum point, $\Delta\lambda_r$ begins to decrease. The electric field distributions $|E_y(x, z)|^2$ near the grating waveguide are plotted in Figure 5-2(c). The left and right panels represent the calculated near field for a-GST and c-GST at $\lambda_r = 1440$ and 1620 nm, respectively. The overlap between the GST layer and the mode region, where the local electric field is strong, determines the amount of wavelength shift induced by the phase transition. In our implementation, the GST film is embedded in the ZnS waveguide with $d_{\text{GST}} \sim 135$ nm to maximize the tuning effect. Meanwhile, the top layer of ZnS can serve as a protection and passivation layer for the GST film.

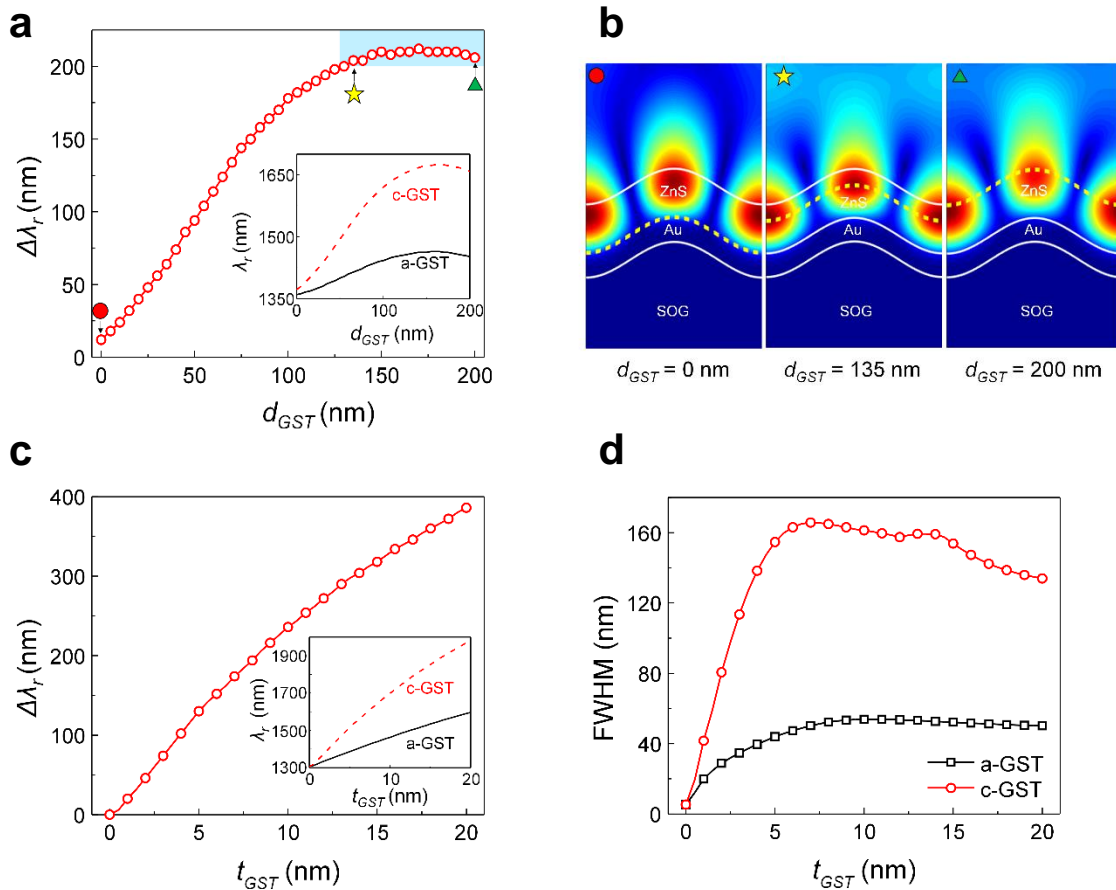


Figure 5-3. Phase change-induced shift of resonance wavelength. (a) Calculated $\Delta\lambda_r$ versus the position of the GST thin film in the 200-nm-thick ZnS waveguide. Inset: the resonant wavelength for GST-PC with amorphous (black solid line) and crystalline GST thin films (red dash line) as a function of d_{GST} . (b) Near-field profiles for GST films located at three different positions ($d_{GST} = 0$ nm, $d_{GST} = 135$ nm and $d_{GST} = 200$ nm). The yellow dash curves denote the location of GST thin film. (c) Calculated $\Delta\lambda_r$ as a function of GST thickness. Inset: the resonant wavelength for GST-PC with amorphous (black solid line) and crystalline GST thin films (red dash line) as a function of t_{GST} . (d) Calculated FWHMs for the GMR modes for the designs with a-GST (black square) and c-GST (red circle), respectively.

The thickness of the GST layer also plays an important role in the tuning capability.

As illustrated in Figure 5-2(a), both real and image parts of the refractive index exhibit significant changes when the GST film switches between the amorphous and crystalline states. It is possible to obtain a sufficient shift to the GMR mode with just a few nanometer-thick GST. On the other hand, a thicker GST film can cause a larger spectral shift. However, since the GST film is lossy at the target wavelength range, an excessively thick GST film

may quench the optical resonance. To investigate the trade-off, we simulated the devices with the t_{GST} ranging from 0 nm to 20 nm. The resonant wavelength as function of t_{GST} for a-GST and c-GST are plotted in Figure 5-3(a). It can be seen that the difference between the a-GST and c-GST resonances increases when the GST film becomes thicker. Figure 5-3(b) summarizes the shift of resonant wavelengths and the full width half maximum (FWHM) of the reflection dips. The FWHM values reach their maximums at $t_{\text{GST}} = 10$ nm for a-GST and $t_{\text{GST}} = 7$ nm for c-GST, respectively. Then, both FWHM curves decrease slightly. This can be explained by the decrease of the GST extinction coefficient (k_{GST}) with the increase of wavelength in the near infrared wavelength range. As the GST thickness increases, the GMR mode shifts to a longer wavelength, where the k_{GST} values decrease for both a-GST and c-GST. The simulation results indicate that as long as the GST thickness is over $t_{\text{GST}} = 10$ nm, a wavelength shift larger than the FWHM of either a-GST or c-GST phase can be ensured. The GST thickness of $t_{\text{GST}} = 10$ nm was selected to achieve the tuning in the desired wavelength range (900 to 1700 nm) with a relatively small FWHM and large wavelength shift.

5.3.2.1 Tuning of GMR mode by the phase transition of GST

Based on the RCWA simulation results, we fabricated the GST-PC device as shown in Figure 5-1(b)-(d). The sinusoidal SOG grating with $\Lambda = 1000$ nm and $d_{\text{GST}} = 150$ nm was fabricated. The gold film ($t_{\text{Au}} = 200$ nm) and ZnS ($t_{\text{ZnS}} = 200$ nm) layers were coated using an e-beam evaporator. The amorphous GST layer ($t_{\text{Au}} = 200$ nm) was deposited between two ZnS layers using a sputter. A testing setup was built to control the phase transition of the GST film and characterize the sample response. As shown in Figure 5-4(a), the device is illuminated by a collimated, TE-polarized broadband light from a fiber in its normal direction. The reflected light is collected by the same fiber and analyzed using a InAsP NIR spectrometer (StellarNet Inc.) for spectral analysis.

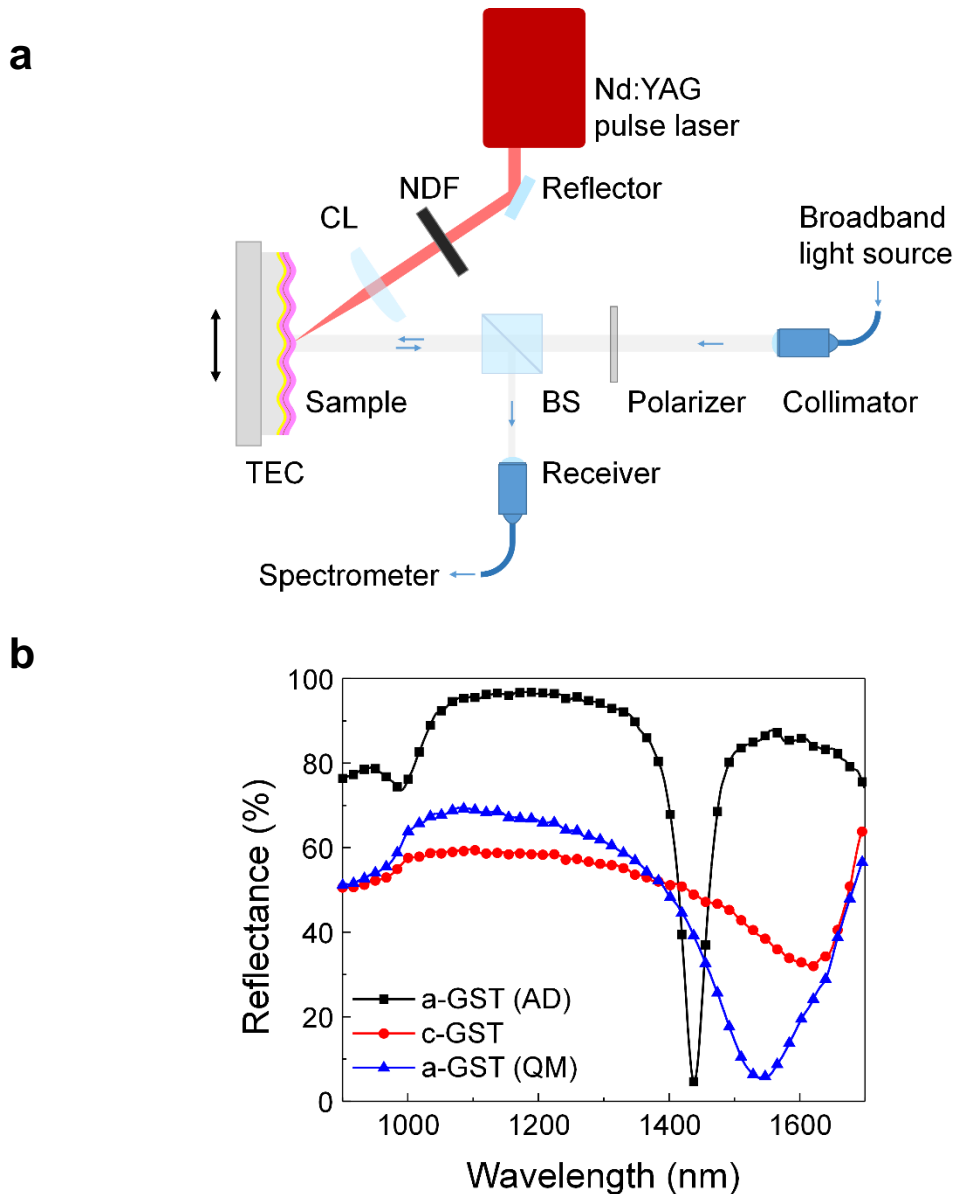
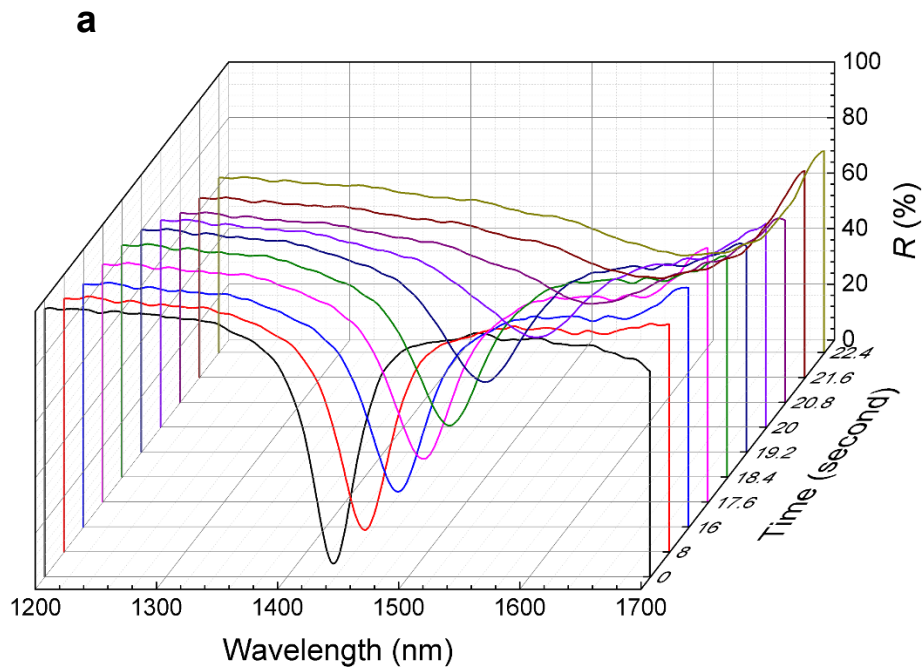


Figure 5-4. (a) Schematic of the optical setup for reflection measurement and laser line-scanning apparatus. The sample is mounted on a thermoelectric cooler (TEC), which can control the sample temperature. The laser line-scanning setup consists of a pulse Nd:YAG laser, a dielectric mirror, a neutral density filter (NDF), and a cylindrical lens (CL). The linearly polarized broadband light is used as the excitation to measure the sample reflection. The reflected light is directed to a near infrared spectrometer using a beam splitter (BS). (b) Measured reflection spectra for the GST-PC with as-deposited a-GST (black), c-GST (red), and melt-quenched GST (blue) layers, respectively.

5.3.2.1.1 Heat-induced crystallization

The reflection spectrum of the device with the sputtered amorphous GST was measured and shown in Figure 5-4(b). To induce its crystallization, the GST film needs to be heated above its crystallization temperature (T_c) but below the melting temperature (T_m). Here, a thermoelectric cooler (TEC) (Marlow, TG12-4L) was used to heat the GST-PC mounted on the hot side of the TEC. We recorded the reflection spectra every 200 ms, right after the TEC was turned on. The measured reflection spectra at some time stamps are shown in Figure 5-5(a). A continuous shift of the GMR mode from 1439 nm to 1610 nm was observed in a time span of 22.4 seconds. The phase transition from a-GST to c-GST also broadens the FWHM of the GMR mode from 53 nm to 210 nm. The results indicate that both n_{GST} and k_{GST} increases with the temperature, as the evidence of an undergoing crystallization process.



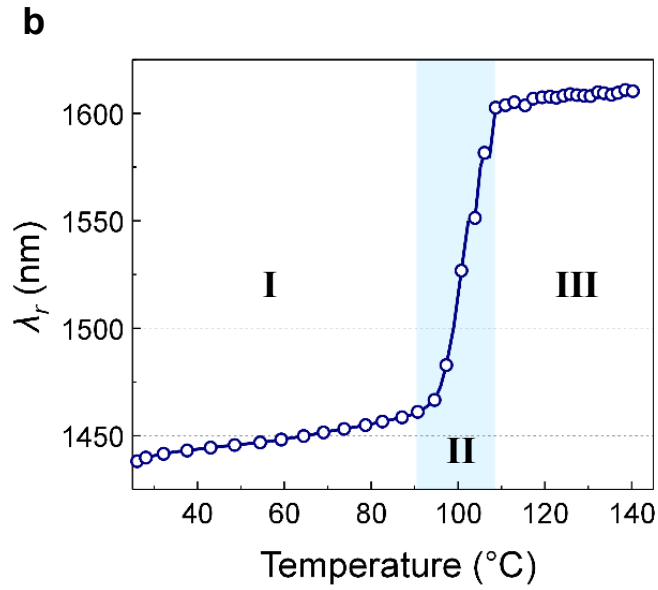


Figure 5-5. Measured GMR mode versus temperature. (a) Waterfall plot of ten selected reflection spectra of GST-PC in the progress when the as-deposited amorphous GST layer was being transitioned into crystalline phase using TEC heating. The spectra were recorded every 200 ms for a period of 45 s. The broadening of the reflection dip was observed. (b) Shift of resonant wavelength as a function of temperature. The resonant wavelength increases dramatically during the phase transition of GST (highlighted by the region shaded in blue).

In the meantime, we recorded the temperature on the device using a thermocouple.

The resonant wavelength vs. temperature curve is plotted in Figure 5-5(b). The resonant wavelengths were found using the peak-finding algorithm (see Experimental Section). It is clear that there are three regions during the temperature raise. In Region I, where the temperature was below 93 °C, the resonance began to shift slowly after the TEC was turned on, from 1439 nm to 1461 nm with a slope of 0.22 nm/°C. Above 93°C, the GMR mode entered the Region II, in which λ_r shifts dramatically from 1461 nm to 1603 nm with a slope as large as 9.33 nm/°C. Then the resonant wavelength gradually became stabilized near 1610 nm in Region III, which suggests that the GST layer has been fully crystallized.

5.3.2.1.2 Pulse laser-induced amorphization

To switch the GST film from its crystalline state back to an amorphous state, it is necessary to heat the GST above its melting temperature and cool it down fast enough to achieve the melt-quenched a-GST film. As already demonstrated in the previous works, ultrafast pulse lasers are well suitable for such a task. In our experiment, we utilized a Q-switched Nd:YAG laser (Oppolette) to obtain amorphization for the c-GST film. The laser output 5 ns laser pulses at 1064 nm with the beam diameter of 3 mm. Due to the spectacles in the laser beam, direct exposure of the device under the laser beam led to spatially non-uniform transition over the device. In order to eliminate the non-uniformity issue, we focused the laser beam into a 3-mm-long and 20-um-wide line using a cylindrical lens (focal length = 35 mm). The laser fluence and repetition rate were set at xx $\mu\text{J}/\text{mm}^2$ and 20 Hz, respectively. The device was mounted on a motorized translation stage and scanned through the laser line in order to expose the desired area. The scanning speed was adjusted to match the repetition rate of the pulse laser. Each scan generated an area of 3 mm \times 3 mm of on the device with the melt-quenched a-GST. The reflection spectrum was measured after the scanning process. Figure 5-5(b) compares the reflectance of the device with the as-deposited a-GST, c-GST, and the melt-quenched a-GST. The reflection dip of melt-quenched a-GST cannot shift back to the position of the as-deposited a-GST. It is already known that melt-quenched a-GST has different electrical and optical properties (Figure 5-2(b)) with as-deposited a-GST.

5.3.2.2 Cycling between *a*-GST and *c*-GST modes

To study the reparability of the GST tuning, we tested the crystallization and melt-quenched amorphization processes, which were repeated for multiple cycles. For each cycle, the device was heated using the TEC and consequentially scanned using the pulse laser. The reflection spectra were recorded every 200 ms during the crystallization, and the recording

was paused during the amorphization. The resonant wavelengths were calculated as a function of time. Results of the first six cycles are summarized in Figure 5-6. The cycling experiment started with the device containing the as-deposited a-GST film. The initial resonant wavelength located at 1440 nm. The first crystallization process shifted the resonant wavelength to 1620 nm and the subsequent melt-quenched process moved the resonance back to 1544 nm. During the following cycles, the resonance wavelength was tuned in the range of 1544 nm to 1592 nm as highlighted in the shadow area in Figure 5-6.

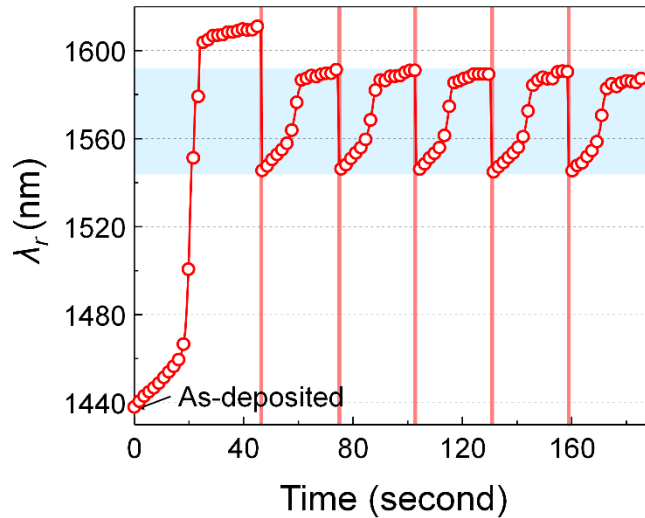


Figure 5-6. Tuning of GMR mode during six cycles of phase transitions. The transitions from c-GST to a-GST are labelled by the vertical blue line, where the sample was scanned by the pulse laser. The substrate temperature was set at room temperature during the re-amorphizations. The sample was heated to GST's crystallization temperature during each cycle and the reflection spectra were measured every 200 ms.

5.4 Conclusion

In summary, we have designed and fabricated a photonic crystal filter based on a multi-layer sinusoidal grating. The filter was incorporated with a thin film of phase-change material, GST, which enabled it to tune its resonant wavelength of the leaky-mode in the near infrared wavelength range. We have utilized RCWA simulation techniques to find out the

optimized GST locations inside the waveguide, as well as the optimum GST thickness. We also designed and built a line-scanning platform on which we successfully induced crystallization for amorphous GST by TEC heating, and re-amorphization for crystallized GST by nanosecond laser pulse. The complex refractive index values, n and k in the 900 ~1700 nm for as-deposited amorphous GST, crystallized GST and melt-quenched amorphous GST were measured using ellipsometry. The cycles of crystallization and amorphization were also demonstrated to prove the reliability and repeatability of our device. In our future work, we'll try to realize all light tuning and electric tuning for the GST-PC device.

5.5 Experimental Section

Fabrication of the GST-tuned filter : Figure S1 summarizes the imprint lithography-based fabrication of the proposed tunable GST-PC filter. First, a polydimethylsiloxane (PDMS) stamp was replicated from a commercial holographic grating with the grating period of 1 μ m (Edmund Optics, #40-267). To fabricate the grating using glass, a few droplets of SOG solution (Honeywell Accuglass 512B) was spun onto a pre-oxidized Si wafer (SiO₂ thickness = 250 nm) at a spin speed of 800 rpm for 10s. Immediately after the spin-coating, the thin SOG film was molded using the PDMS stamp under a pressure of 80 KPa. The sample, together with the PDMS stamp, was baked at 65 °C on a hotplate for 3 mins to solidify the SOG film. After the PDMS stamp was peeled away, the sinusoidal grating was produced in the SOG film. Then, the sample was post-baked on a hotplate at 220 °C overnight to completely solidify the SOG. Finally, the sample was deposited with a stack of Au/ZnS/GST/ZnS thin films using an e-beam evaporator (Temescal) for the Au and ZnS layers and a sputter machine (AJA) for the GST layer.

Reflection measurement setup: Reflection measurements of the GST-PCs were carried out using an optical setup shown in Figure 5-4(a). The output a 100 W halogen light source

(OceanOptics) was collimated using a fiber-tip collimator (Thorlabs Inc.) and polarized using a linear polarizer. The TE-polarized beam was incident onto the GST-PC device via a non-polarizing 50/50 beam splitter cube. The reflected light was directed to a fiber coupled near-infrared spectrometer (SpectraNet, Inc.). The spectral range of the spectrometer is 897 nm to 1788 nm. The reflectance (R) was calculated against a gold-coated mirror as the reference. To identify the resonant wavelength, we used a second polynomial function to fit 20 data points near the minimal transmittance point. During the experiment, the reflection spectra were continuously recorded.

Line-scanning setup for the re-amorphization of GST: As shown in Figure 5-4(a), a Q-switched Nd:YAG pulse laser (Opoptette) with emission wavelength of 1064 nm and pulse duration of 5 ns at a maximum repetition rate of 20 Hz was utilized for the re-amorphization of the GST thin film inside the GST-PC device. The pulse laser was focused into a 3-mm long line (width \approx 20 μ m) using a cylindrical lens with a focal length of 35 mm. The GST-PC was mounted on a kinematic mount with a TEC attached to its back side. A thermocoupler was also attached to the top surface of the device to monitor the real-time temperature. The GST-PC was carefully placed to ensure its top surface is at the focal plane of the cylindrical lens. The whole fixture was mounted on a motorized linear translation stage (ASI Instrument), with the translation direction perpendicular to the focused laser line. In order to scan a continuous rectangular patch on the GST-PC surface, the pulse repetition rate and the move speed of the translation stage was synchronized, at 20 Hz and 0.3 mm/s, respectively. The actual fluence needed to melt the GST layer varied from sample to sample, while still stayed in a small range. For samples demonstrated in this paper, with a GST thickness of 8.5 nm, we used 285 mJ/cm⁻² fluence for re-amorphization.

Numerical modeling: Rigorous coupled wavelength analysis (DiffractMOD, RSoft, Synopsys Inc.) was used to numerically characterize the optical responses of the GST-PC devices. The 2D GST-PC structure was illuminated with a normally incident, unit magnitude, TE-polarized plane wave propagating in the direction ($-z$ -axis), which is perpendicular to the sample surface. The simulation domain was set to one-unit cell of the periodic grating structure along the x -direction. The optical properties of Au were taken from Johnson and Christy's handbook.⁷⁶ The refractive index and extinction coefficient of the GST (a-GST and c-GST) were from the results of ellipsometry measurement and fitted by the multi-coefficient Lorentz-Drude model in the wavelength range from 900 nm to 1700 nm.

5.6 Acknowledgements

This work was supported by the National Science Foundation under Award No. ECCS 09-24062. Any opinions, findings, and conclusions or recommendations expressed in this material are those of the author(s) and do not necessarily reflect the views of the National Science Foundation. LL acknowledges the Catron Foundation Graduate Fellowship for financial support. We would like to thank Dr. Liang Dong for providing the pulse laser and the room for the optical setup. The authors declare no competing financial interests.

CHAPTER 6. ULTRATHIN FREESTANDING PLASMONIC MEMBRANES

6.1 Abstract

We demonstrate an ultra-thin freestanding plasmonic membrane that supports surface plasmon resonances. The 30 nm-thick membrane is perforated with an array of holes using the imprint-and-transfer approach. The fabricated plasmonic membrane exhibits extraordinary optical transmissions (EOT) in the mid-wave infrared wavelength range and can be used as an optical sensor to measure the absorption of a thin polymer film.

6.2 Introduction

In this paper, we demonstrate an ultra-thin freestanding gold plasmonic membrane perforated with an array of subwavelength holes, which supports extraordinary optical transmission (EOT) in the mid-wavelength infrared range. The 30-nm thick membrane was fabricated using an imprint-and-transfer technique based on soft imprint lithography. The fabricated gold plasmonic membrane was suspended over a metal grid. The EOT resonant modes supported by the plasmonic membrane were tuned within the mid-wavelength infrared range by varying incident angle. At last, by leveraging the angular dispersion of plasmonic resonances and the chemical specificity of vibrational spectroscopy, we utilized the plasmonic membrane as a surface-based optical sensor to performed real-time and label-free detection for two C=H stretching modes of a dip-coated thin layer of polyvinyl copolymer. Experimental results show plasmon resonance enhanced infrared absorption as a result of the interactions of surface plasmon polaritons and C=H stretching modes.

6.3 Results and Discussion

6.3.1 Structure of plasmonic membrane

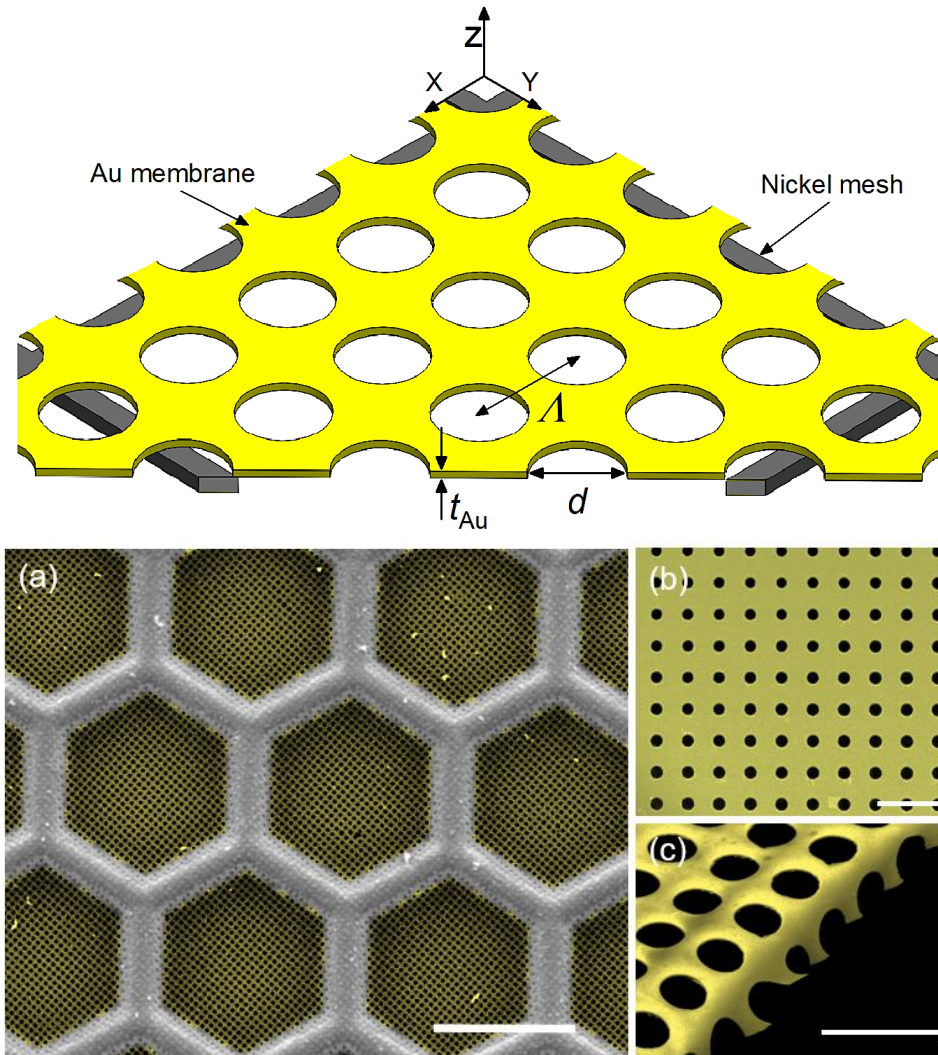
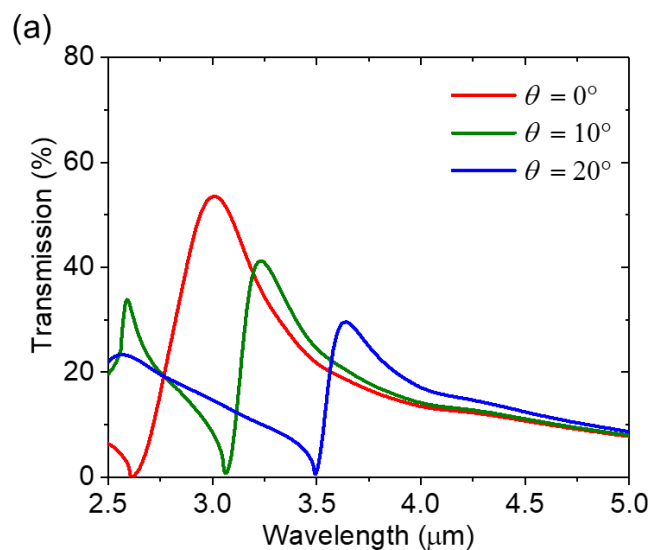


Figure 6-1. (a) Schematic of the freestanding plasmonic membrane (not on scale). The incident and transmission light beams are in z direction. SEM images of the fabricated plasmonic membrane. (a) Membrane on a mesh. (b) Plasmonic membrane with $\Lambda = 2.5 \mu\text{m}$, $d = 1.25 \mu\text{m}$, and $t_{\text{Au}} = 30 \text{ nm}$. (c) SEM of the cross-section of the gold membrane. Scale bar: (a) $100 \mu\text{m}$; (b) and (c) $5 \mu\text{m}$.

Figure 6-1(a) shows a schematic illustration of the ultra-thin plasmonic membrane comprised of a freestanding gold film with a two dimension (2D) square lattice of sub-wavelength holes. The membrane is suspended over the $100 \mu\text{m}$ -diameter apertures of a nickel mesh. The geometry of this membrane, including period (Λ), hole diameter (d), and

membrane thickness (t_{Au}), can be designed to manifest plasmon resonances in a desired wavelength range.

We employed FDTD simulation to calculate the angle-dependent transmission behaviors of the FPM. Figure 6-2(a) shows simulated transmission spectra of the FPM for different angles of incidence under p -polarized illumination. The FPM exhibits significantly enhanced optical transmission, and the distinct plasmon resonance peaks, which are respectively labeled by the red, green and blue dots, appear with a considerable red shift and decreased amplitude when the angle of incidence increases. Stimulated field intensity distributions associated with the indicated plasmon resonances are shown in Figure 6-2(b) and (c), respectively. The color bar on the right side is scaled by the normalization of electric field intensity ($|E|^2$) to the incident electric field intensity ($|E_{inc}|^2$). It can be seen that there is significant field enhancement at the metal-air interface in the regions between the holes. The strongly confined resonant modes spatially overlap the medium residing inside the hole, indicates that the FPM could be used for an optical sensor to measure the absorption of the medium, which relies on large local field enhancements.



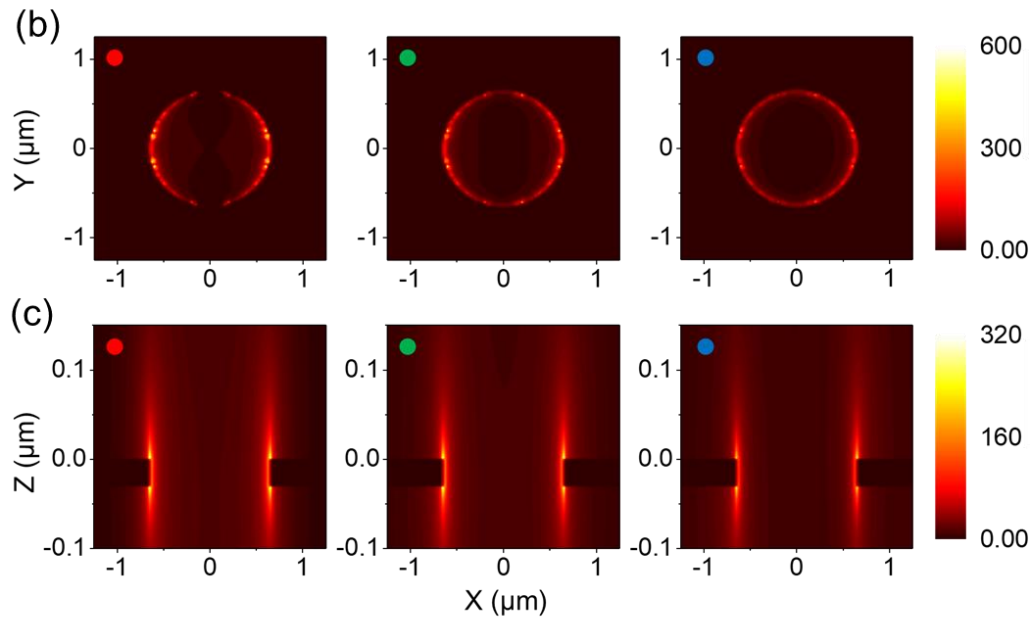


Figure 6-2. Angular dependence of the optical transmissions and near field distributions of the FPM. (a) Simulated transmission spectra for different incident angles under p -polarized illumination. (b) and (c) the top-view (x - y plane) and cross-sectional view (x - z plane) of spatial electric-field intensity enhancement profiles within one unit volume of the FPM for the indicated plasmon modes.

6.3.2 Fabrication of the membrane: imprint and transfer

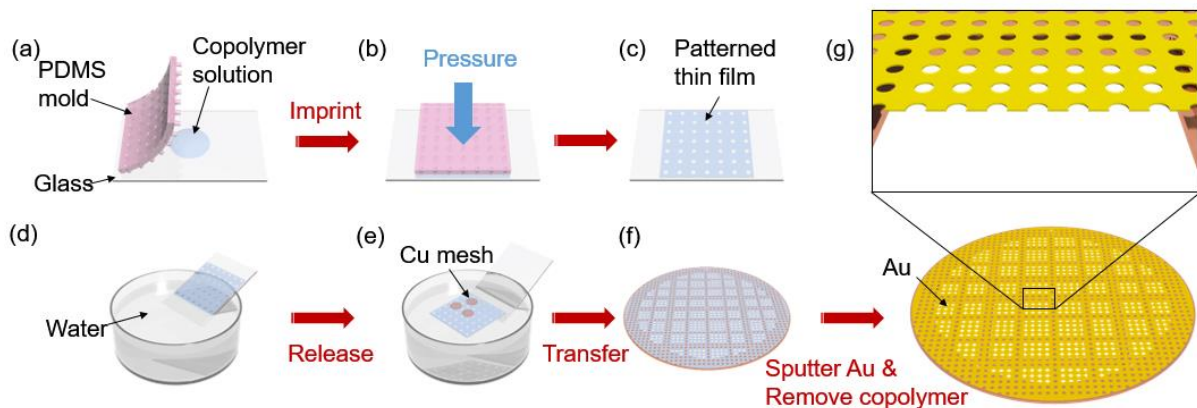


Figure 6-3. Fabrication process flowchart for the freestanding plasmonic membrane. The imprint-and-transfer approach was used to generate the patterned membranes inexpensive.

As summarized in Figure 6-3, the fabrication process of the plasmonic membrane consists of three major steps: imprint, transfer, and thin-film coating. Before imprint, a

PDMS stamp was prepared by molding from a silicon wafer bearing the 2D array of nano-wells. The array pattern was first transferred to a 50 nm-thick polymer film by squeezing a low viscosity copolymer of 0.5% poly (vinyl formal) between the PDMS stamp and a glass slide. After imprinting, the patterned polymer film was transferred from the glass slide to the surface of water in a beaker. The surface tension of water helped to release and support the copolymer film. We placed the nickel mesh on the polymer film and carefully picked up the mesh. The sample was baked (at 100°C) to assure that the polymer membrane was fully perforated. Finally, a 30 nm thick film of gold was deposited over the polymer membrane and the copolymer membrane was removed by soaking the sample in dichloroethene.

6.3.3 Characterization for plasmonic membrane

6.3.3.1 Transmission spectrum and EOT

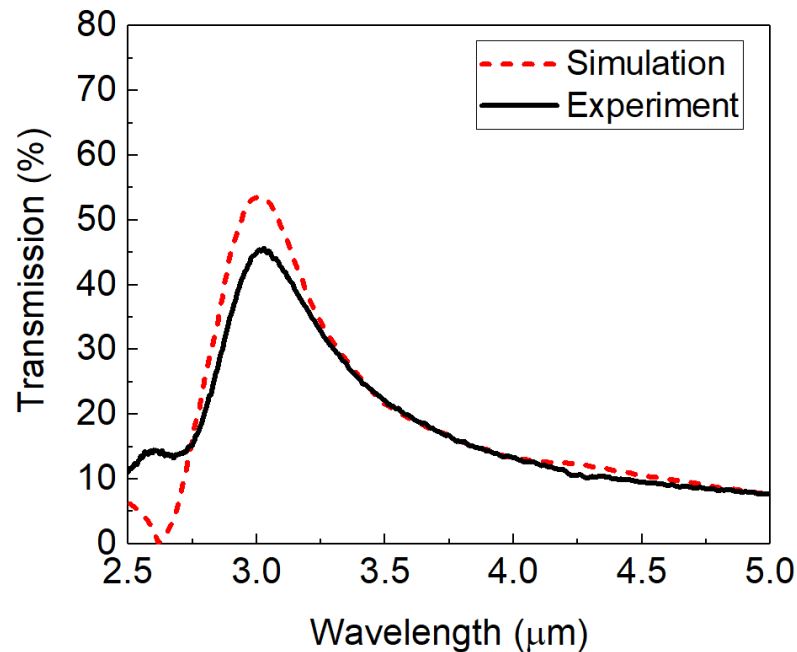


Figure 6-4. EOT spectrum at normal incidence compared with simulation

The plasmon resonances of the device were modeled using a Fourier transform infrared spectrometer. The simulation and measurement results are compared in Figure 6-4 at

normal incidence. The measured transmission spectra show very good spectral agreement with simulation results. The plasmonic membrane exhibits significantly enhanced peak transmission at the resonant wavelength (λ_r). When normalized to the same mesh without the metal membrane, the peak transmission reaches 70% for the normal incidence case. The resonant wavelength increases with the change of the incident angle. When $\theta = 0^\circ$, 10° , and 20° , the resonant wavelength are $2.94 \mu\text{m}$, $3.21 \mu\text{m}$, and $3.60 \mu\text{m}$ respectively. The angular dispersion of the EOT structure is approximately $33 \text{ nm}/^\circ$. As the incident angle moves away from normal, we observe a decrease in the transmission coefficients, which is expected for incident light with a wave vector in the direction of SPP propagation. During the tests, the incident light was TM polarized with the electric field component parallel to the incident plane.

6.3.3.2 Effect of membrane thickness on EOT

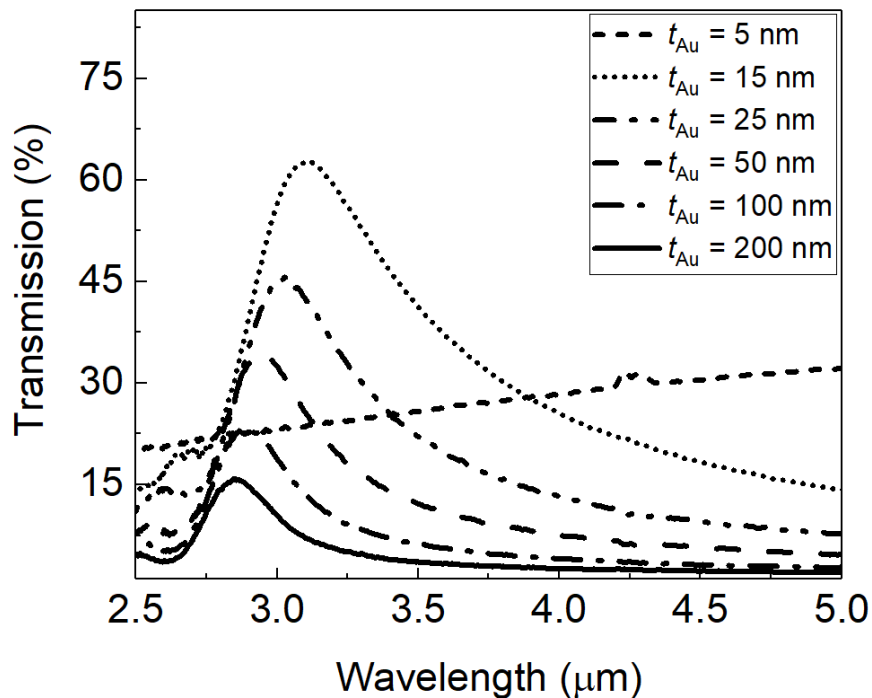


Figure 6-5. The effect of membrane thickness on EOT spectra

The effect of gold thickness on the transmission spectra was studied over a Mid-infrared range (2.5- 5 μ m) using Varian FTS 7000 FT-IR and a polarized light. The influence of 0, 5, 15, 25, 50, 100 and 200 nm-thick gold layer on transmission spectra of the Au-membrane is compared in Figure 6-5 for the normal incidents. As can be seen, for the gold thickness below 15 nm no plasmonic resonance observed neither in normal or angled incidents. Increasing the gold thickness introduces more conduction electrons to oscillate which enhance surface plasmon resonance (SPR). Further increase of the gold layer thickness, up to 200 nm, results in lowering the resonance wavelength from 3.12 to 2.87 μ m. Furthermore, with 15 nm of gold thickness at normal incidence, a full width at half maximum (FWHM) of 0.56 μ m was calculated, however, this value dropped to 0.22 μ m at the gold thickness of 200 nm. As a result, increasing the gold thickness narrows down the peak.

6.3.3.3 Angular dispersed measurement

Angular transmission resonances of Au-membrane samples coated with different gold thickness was investigated in Mid-infrared range using FT-IR and a rotational stage as demonstrated in figure 5. A linear polarizer located at incident light aperture with the electric field component parallel to the incident plane and a rotational stage was mounted between the incident light and the detector aperture. Angular transmission resonances of the specimens coated with 5, 15, 25, and 50 nm of gold are shown in Figure 6-6. The resonance wavelength of the normal and 30° incidents for the Au-membrane coated with 13 nm of gold is 3.1 and 4.16 μ m respectively. The difference between the normal and 30° incident increases from 1.06 to 1.16 μ m by thickened the gold layer from 13 to 205 nm, as a result, thinner gold layer lower the angular dependency of the resonance wavelength.

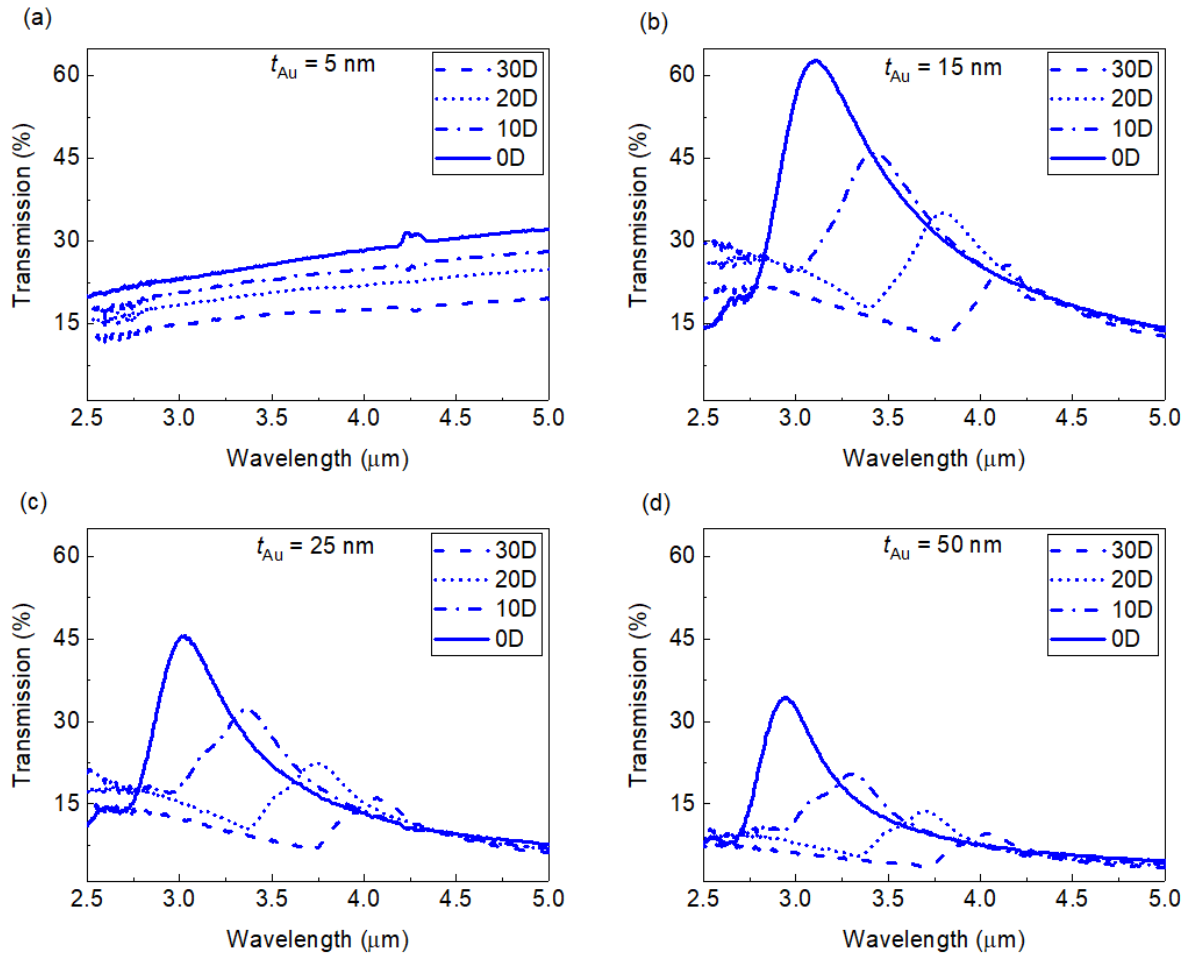


Figure 6-6. Angular dispersed measurement of membrane with different thickness at 5 nm, 15 nm, 25 nm and 50 nm.

6.3.4 Surface enhanced infrared absorption spectroscopy (SEIRA)

The infrared FPM offers remarkable opportunities for exploration of surface-based sensors. As an example, we adopted the FPM to characterize the coating of a thin copolymer film. The FPM was coated with a thin layer of copolymer by dipping the device into a copolymer solution and pulled out, followed by air-drying.

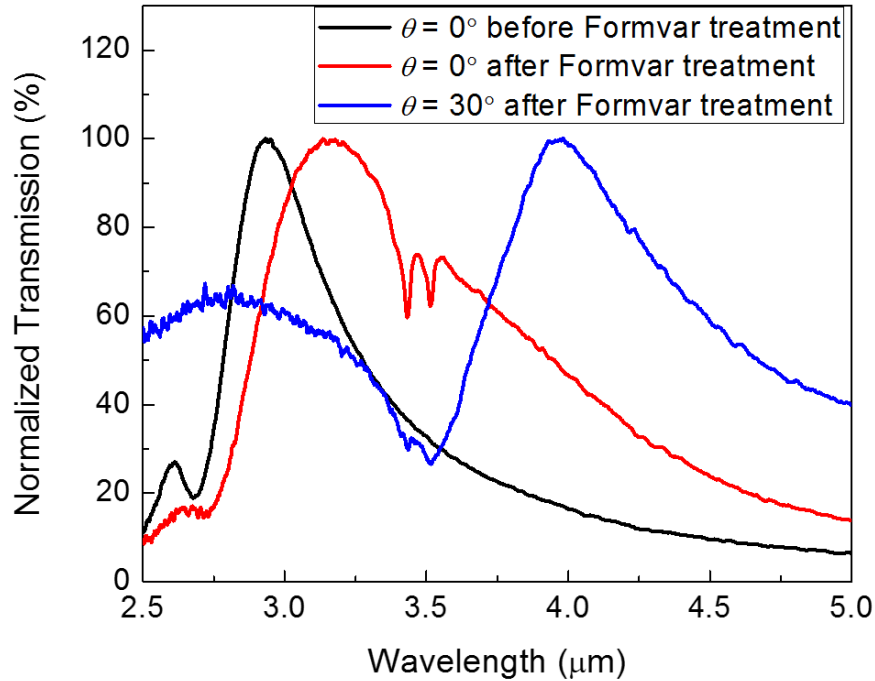


Figure 6-7. EOT before and after coating of copolymer.

As shown in Figure 6-7, the coating results in a shift of the EOT peak by 220 nm. The phenomena can be exploited for a refractive index-based label-free detection. In addition, the plasmonic membrane is capable of enhancing the chemical specific absorption in infrared, owing to the strengthened near field around the membrane. By comparing the measurements at $\theta_i = 0^\circ, 10^\circ, 20^\circ$ and 30° shown in Figure 6-7, it can be seen that the absorption CH_2 stretching modes (2950 cm^{-1} and 2994 cm^{-1}) is significantly enhanced when vibrational modes of analyte fall in the plasmonic resonance.

6.4 Conclusion

In this work, we have developed and optimized a nanoimprint lithography method using a copolymer of poly(vinyl formal) as the resin to fabricate a ultrathin freestanding plasmonic membrane.

6.5 Experimental Section

Fabrication of freestanding plasmonic membrane with subwavelength hole-array:

(1) Imprint: A polydimethylsiloxane (PDMS) stamp (1.8 cm×1.2 cm) was replicated from a silicon master carrying a 2D array of subwavelength wells. The copolymer solution was prepared by dissolving powders of poly (vinyl formal) in dichloromethane (0.5% w/v) and mixing using a vortex mixer. During the imprinting process, 5 μ L of the copolymer solution was dropped onto a pre-cleaned glass slide, and immediately spread by pressing the PDMS stamp against it. 8.3 kPa pressure was applied by placing an aluminum block on top of the stamp for 5 minutes to let the solvent evaporate completely. The PDMS stamp was then removed carefully, leaving a solidified thin film of copolymer patterned with a 2D array of subwavelength hole array on the glass slide.

(2) Transfer: Next, copolymer thin film was released on water surface by inserting the glass slide into a beaker of warm water at a small angle. Then 4~6 copper or nickel meshes were placed upon the substrate-free film, and a new glass slide was dipped into the water to pick up the copolymer film and dried in air for 10 mins. The meshes were sandwiched between the thin film and the glass slide.

(3) Metallization: Next, the device was baked at 100°C in a vacuum oven for 10 mins to make sure every hole on the copolymer film was perforated. Finally, the device was coated with 30 nm thick gold by sputtering (Denton Desktop IV) and then immersed into dichloromethane again to remove the copolymer supporting layer.

Optical Characterization using FTIR:

A schematic of the optical layout inside the measurement chamber is illustrated in Figure 6-8. The FPM was mounted on a rotation stage inside the measurement chamber of a FTIR platform. The FPM can be rotated in the x - y plane, the angle between its normal and

the x -axis defines the launch angle θ . As shown in Figure 6-8(b), the hole array on the FPM is aligned with the y - and z - axis when θ is zero. The IR illumination comes in the $+x$ direction. A polarizer is used to make the illumination TM-polarized, or paralleled with the x - y plane. The transmitted IR light was collected using a deuterated-triglycine sulfate (DTGS) detector.

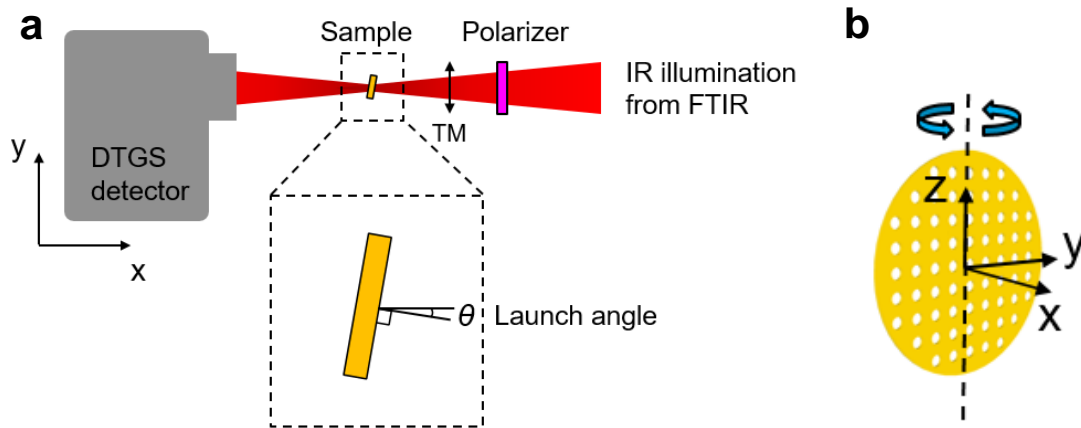


Figure 6-8. Schematic of the optical characterization using FTIR for the freestanding plasmonic membrane. (a) The setup inside the FTIR chamber (b) The orientation of the hole arrays on the freestanding plasmonic membrane

Numerical modeling: 3D FDTD simulations were carried out to model the optical transmission and the near-field profile of the FPM. The workspace for the simulation was set to have a length of one period in both x - and y - axes, with periodic boundary condition applied. The light source was chosen to be a unit plane wave coming along the z -axis, with perfectly matched layer (PML) boundary condition imposed at the boundaries. A frequency domain field and power monitor was placed close to the PML boundary for the calculation of transmittance of the device.

Copolymer coating:

The FPM was dipped vertically into a solution of the copolymer with a w/v concentration of 0.1% for 5 seconds, then quickly pulled out and put aside for 10 mins to let it air dry.

CHAPTER 7. CONCLUSION AND OUTLOOK

In summary, the fabrication, instrumentation and applications of subwavelength periodic nanostructure was investigated. Firstly, we have designed and built a low-cost angular dispersion detection instrument based on a PC slab sensor for refractometric sensing and imaging. A focused He-Ne laser beam was utilized to monitor precisely the changes of GMR resonant angle. The optical arrangement adopted in this platform provides flexible selection of detection range and adjustable angular resolution. The capability for mapping a patterned thin dielectric film on a PC sensor up to a spatial resolution of $10\ \mu\text{m}$ has been demonstrated.

Secondly, we developed a novel programmable nanoimprint lithography method that improves the fabrication of grating-based nanophotonic devices. Utilizing this method, sub-wavelength periodic nanostructures with various pre-designed lattice constants or lattice arrangements can be obtained out of a single elastomeric mold. Following this strain-tunable nanoimprint lithography method, we have successfully generated a 1D grating pattern with a graded period along the stretching direction on a device surface, resulting in a linear variable photonic crystal filter with a continuously varying resonant wavelength along its surface.

Thirdly, we have also designed and fabricated a tunable photonic crystal filter based on a multi-layer sinusoidal grating. By incorporating a phase-change material, GST, thin film, we successfully tuned its resonant wavelength of GMR in the near infrared wavelength range. Numerical calculations were carried out to optimize the dimension parameters of the proposed GST-PC. We also designed and built a line-scanning used to induce phase transitions for the GST thin film. In our future work, we'll try to realize all light tuning and electric tuning for the GST-PC device.

REFERENCES

1. Busch, K. *et al.* Periodic nanostructures for photonics. *Phys. Rep.* **444**, 101–202 (2007).
2. Chou, S. Y. Nanoimprint lithography. *J. Vac. Sci. Technol. B Microelectron. Nanom. Struct.* **14**, 4129 (1996).
3. Zhao, X.-M., Xia, Y. & Whitesides, G. M. Soft lithographic methods for nano-fabrication. *J. Mater. Chem.* **7**, 1069–1074 (1997).
4. George, M. C. *et al.* Wafer-scale plasmonic and photonic crystal sensors. *Proc. SPIE* **9547**, 95471F (2015).
5. Lu, C. & Lipson, R. H. Interference lithography: A powerful tool for fabricating periodic structures. *Laser Photonics Rev.* **4**, 568–580 (2010).
6. Pokhriyal, A. *et al.* Photonic crystal enhanced fluorescence using a quartz substrate to reduce limits of detection. *Opt. Express* **18**, 24793–808 (2010).
7. Lu, M., Choi, S. S., Irfan, U. & Cunningham, B. T. Plastic distributed feedback laser biosensor. *Appl. Phys. Lett.* **93**, (2008).
8. Lee, H. S., Kim, D. S. & Kwon, T. H. UV nano embossing for polymer nano structures with non-transparent mold insert. *Microsyst. Technol.* **13**, 593–599 (2007).
9. Kooy, N., Mohamed, K., Pin, L. T. & Guan, O. S. A review of roll-to-roll nanoimprint lithography. *Nanoscale Res. Lett.* **9**, 1–13 (2014).
10. Ahn, S. H. & Guo, L. J. Large-area roll-to-roll and roll-to-plate Nanoimprint Lithography: A step toward high-throughput application of continuous nanoimprinting. *ACS Nano* **3**, 2304–2310 (2009).
11. Liu, L., Khan, H. A., Li, J., Hillier, A. C. & Lu, M. A strain-tunable nanoimprint lithography for linear variable photonic crystal filters. *Nanotechnology* **27**, (2016).
12. Dobbs, D. W., Gershkovich, I. & Cunningham, B. T. Fabrication of a graded-wavelength guided-mode resonance filter photonic crystal. *Appl. Phys. Lett.* **89**, (2006).
13. Qian, L. *et al.* Electrically driving bandwidth tunable guided-mode resonance filter based on a twisted nematic liquid crystal polarization rotator. *Opt. Lett.* **40**, 713–716 (2015).
14. Wang, Q. *et al.* Type of tunable guided-mode resonance filter based on electro-optic characteristic of polymer-dispersed liquid crystal. *Opt. Lett.* **35**, 1236–1238 (2010).

15. Pi, S. *et al.* Dielectric-Grating-Coupled Surface Plasmon Resonance From the Back Side of the Metal Film for Ultrasensitive Sensing. *IEEE Photonics J.* **8**, 1–7 (2016).
16. Choi, C. J., Xu, Z., Wu, H. Y., Liu, G. L. & Cunningham, B. T. Surface-enhanced Raman nanodomains. *Nanotechnology* **21**, (2010).
17. Wuttig, M. & Yamada, N. Phase Change Materials for Rewriteable Data Storage. *Hg. v. Nat. Mater.* **6**, 824–832 (2007).
18. Kim, S.-Y., Kim, S. J., Seo, H. & Kim, M. R. Variation of the complex refractive indices with Sb-addition in Ge-Sb-Te alloy and their wavelength dependence. 112–115 (1998). doi:10.1117/12.327935
19. Raoux, S. Phase Change Materials. *Annu. Rev. Mater. Res.* **39**, 25–48 (2009).
20. Cunningham, A. J. *Introduction to bioanalytical sensors*. (Wiley New York:, 1998).
21. Vo-Dinh, T. *et al.* *Optical Sensors: Industrial Environmental and Diagnostic Applications*. **1**, (Springer, 2004).
22. Fan, X. *et al.* Sensitive optical biosensors for unlabeled targets: A review. *Anal. Chim. Acta* **620**, 8–26 (2008).
23. Washburn, A. L. & Bailey, R. C. Photonics-on-a-chip: recent advances in integrated waveguides as enabling detection elements for real-world, lab-on-a-chip biosensing applications. *Analyst* **136**, 227–236 (2011).
24. Aksu, S. *et al.* High-throughput nanofabrication of infrared plasmonic nanoantenna arrays for vibrational nanospectroscopy. *Nano Lett.* **10**, 2511–2518 (2010).
25. Armani, A. M., Kulkarni, R. P., Fraser, S. E., Flagan, R. C. & Vahala, K. J. Label-free, single-molecule detection with optical microcavities. *Science (80-.)*. **317**, 783–787 (2007).
26. Cunningham, B. T. & Laing, L. Microplate-based, label-free detection of biomolecular interactions: Applications in proteomics. *Expert Rev. Proteomics* **3**, 271–281 (2006).
27. Magnusson, R., Wawro, D., Zimmerman, S. & Ding, Y. Resonant photonic biosensors with polarization-based multiparametric discrimination in each channel. *Sensors* **11**, 1476–1488 (2011).
28. Chaudhery, V. *et al.* Line-scanning detection instrument for photonic crystal enhanced fluorescence. *Opt. Lett.* **37**, 2565–2567 (2012).
29. Block, I. D. *et al.* A detection instrument for enhanced-fluorescence and label-free imaging on photonic crystal surfaces. *Opt. Express* **17**, 13222 (2009).

30. Li, P. Y., Lin, B., Gerstenmaier, J. & Cunningham, B. T. A new method for label-free imaging of biomolecular interactions. *Sensors Actuators, B Chem.* **99**, 6–13 (2004).
31. Lu, M., Choi, S. S., Wagner, C. J., Eden, J. G. & Cunningham, B. T. Label free biosensor incorporating a replica-molded, vertically emitting distributed feedback laser. *Appl. Phys. Lett.* **92**, (2008).
32. Rothenhäusler, B. & Knoll, W. Surface plasmon microscopy. *Nature* **332**, 615–617 (1988).
33. Luo, S., Chen, L., Bao, Y., Yang, N. & Zhu, Y. Non-polarizing guided-mode resonance grating filter for telecommunications. *Optik (Stuttg)*. **124**, 5158–5160 (2013).
34. Gallegos, D. *et al.* Label-free biodetection using a smartphone. *Lab Chip* **13**, 2124 (2013).
35. Ju, J., Han, Y., Seok, J. & Kim, S. Development of low-cost and large-area nanopatterned vitreous carbon stamp for glass nanoreplication. in *2012 12th IEEE International Conference on Nanotechnology (IEEE-NANO)* 1–4 (2012). doi:10.1109/NANO.2012.6322076
36. Ju, J., Lim, S., Seok, J. & Kim, S. A method to fabricate Low-Cost and large area vitreous carbon mold for glass molded microstructures. *Int. J. Precis. Eng. Manuf.* **16**, 287–291 (2015).
37. Ghaemi, H. F., Thio, T., Grupp, D. E., Ebbesen, T. W. & Lezec, H. J. Surface plasmons enhance optical transmission through subwavelength holes. *Phys. Rev. B* **58**, 6779–6782 (1998).
38. Chang, S.-H., Gray, S. K. & Schatz, G. C. Surface plasmon generation and light transmission by isolated nanoholes and arrays of nanoholes in thin metal films. *Opt. Express* **13**, 3150 (2005).
39. Wang, S. S., Moharam, M. G., Magnusson, R. & Bagby, J. S. Guided-mode resonances in planar dielectric-layer diffraction gratings. *J. Opt. Soc. Am. A* **7**, 1470 (1990).
40. Magnusson, R. & Shokooh-Saremi, M. Widely tunable guided-mode resonance nanoelectromechanical RGB pixels. *Opt. Express* **15**, 10903–10910 (2007).
41. Johnson, S. G., Fan, S., Villeneuve, P. R., Joannopoulos, J. D. & Kolodziejski, L. A. Guided modes in photonic crystal slabs. *Phys. Rev. B* **60**, 5751–5758 (1999).
42. Liu, J.-N., Schulmerich, M. V., Bhargava, R. & Cunningham, B. T. Sculpting narrowband Fano resonances inherent in the large-area mid-infrared photonic crystal microresonators for spectroscopic imaging. *Opt. Express* **22**, 18142 (2014).

43. Ondič, L. *et al.* Diamond photonic crystal slab: Leaky modes and modified photoluminescence emission of surface-deposited quantum dots. *Sci. Rep.* **2**, 1–6 (2012).
44. Zhao, S. *et al.* Mechanical stretch for tunable wetting from topological PDMS film. *Soft Matter* **9**, 4236 (2013).
45. Lin, P.-C., Vajpayee, S., Jagota, A., Hui, C.-Y. & Yang, S. Mechanically tunable dry adhesive from wrinkled elastomers. *Soft Matter* **4**, 1830 (2008).
46. Emadi, A. *et al.* Fabrication and characterization of IC-Compatible Linear Variable Optical Filters with application in a micro-spectrometer. *Sensors Actuators, A Phys.* **162**, 400–405 (2010).
47. Piegari, A. & Bulir, J. Variable narrowband transmission filters with a wide rejection band for spectrometry. *Appl. Opt.* **45**, 3768–3773 (2006).
48. Piegari, A., Bulir, J. & Krasilnikova Sytchkova, A. Variable narrow-band transmission filters for spectrometry from space. 2. Fabrication process. *Appl. Opt.* **47**, C151–6 (2008).
49. Kiesel, P., Schmidt, O., Mohta, S., Johnson, N. & Malzer, S. Compact, low-cost, and high-resolution interrogation unit for optical sensors. *Appl. Phys. Lett.* **89**, (2006).
50. Emadi, A., Wu, H., de Graaf, G. & Wolffenbuttel, R. Design and implementation of a sub-nm resolution microspectrometer based on a Linear-Variable Optical Filter. *Opt. Express* **20**, 489 (2012).
51. Ding, Y. & Magnusson, R. Use of nondegenerate resonant leaky modes to fashion diverse optical spectra. *Opt. Express* **12**, 1885–1891 (2004).
52. Sharon, a., Rosenblatt, D. & Friesem, a. a. Resonant grating–waveguide structures for visible and near-infrared radiation. *J. Opt. Soc. Am. A* **14**, 2985 (1997).
53. Uddin, M. J. & Magnusson, R. Efficient guided-mode-resonant tunable color filters. *IEEE Photonics Technol. Lett.* **24**, 1552–1554 (2012).
54. Block, I. D., Ganesh, N., Lu, M. & Cunningham, B. T. A Sensitivity Model for Predicting Photonic Crystal Biosensor Performance. *IEEE Sens. J.* **8**, 274–280 (2008).
55. Day, R. W., Wang, S. S. & Magnusson, R. Filter-response line shapes of resonant waveguide gratings. *J. Light. Technol.* **14**, 1815–1824 (1996).
56. Xia, Y. Soft Lithography. *Angew. Chemie (International ed.)* **37**, 551–575 (1998).
57. Ganesh, N., Xiang, A., Beltran, N. B., Dobbs, D. W. & Cunningham, B. T. Compact wavelength detection system incorporating a guided-mode resonance filter. *Appl. Phys. Lett.* **90**, (2007).

58. Niraula, M., Yoon, J. W. & Magnusson, R. Mode-coupling mechanisms of resonant transmission filters. *Opt. Express* **22**, 25817 (2014).
59. Liu, J.-N., Schulmerich, M. V., Bhargava, R. & Cunningham, B. T. Optimally designed narrowband guided-mode resonance reflectance filters for mid-infrared spectroscopy. *Opt. Express* **19**, 24182 (2011).
60. Uddin, M. J., Khaleque, T. & Magnusson, R. Guided-mode resonant polarization-controlled tunable color filters. *Opt. Express* **22**, 12307 (2014).
61. Wawro, D., Tibuleac, S., Magnusson, R. & Liu, H. Optical fiber endface biosensor based on resonances in dielectric waveguide gratings. *Proc. SPIE - Int. Soc. Opt. Eng.* **3911**, 86–94 (2000).
62. Mehta, A. A., Rumpf, R. C., Roth, Z. A. & Johnson, E. G. Guided mode resonance filter as a spectrally selective feedback element in a double-cladding optical fiber laser. *IEEE Photonics Technol. Lett.* **19**, 2030–2032 (2007).
63. Polman, A. & Atwater, H. A. Photonic design principles for ultrahigh-efficiency photovoltaics. *Nat. Mater.* **11**, 174–177 (2012).
64. Chaudhery, V., George, S., Lu, M., Pokhriyal, A. & Cunningham, B. T. Nanostructured surfaces and detection instrumentation for photonic crystal enhanced fluorescence. *Sensors (Switzerland)* **13**, 5561–5584 (2013).
65. Chen, W. *et al.* Photonic crystal enhanced microscopy for imaging of live cell adhesion. *Analyst* **138**, 5886–5894 (2013).
66. Niraula, M., Yoon, J. W. & Magnusson, R. Single-layer optical bandpass filter technology. *Opt. Lett.* **40**, 5062–5065 (2015).
67. Ohta, T. Phase-change optical memory promotes the DVD optical disk. *J. Optoelectron. Adv. Mater.* **3**, 609–626 (2001).
68. Group, F. P. D. & Innovation, N. Phase-Change Meta-materials for future PCRAM Contents :
69. Burr, G. W. *et al.* Phase change memory technology. **28**, 223–262 (2010).
70. Appavoo, K. & Haglund, R. F. Polarization selective phase-change nanomodulator. *Sci. Rep.* **4**, 1–6 (2014).
71. Wetnic, W. & Wuttig, M. Reversible switching in phase-change materials. *Mater. Today* **11**, 20–27 (2008).
72. Yoo, S., Gwon, T., Eom, T., Kim, S. & Hwang, C. S. Multicolor Changeable Optical Coating by Adopting Multiple Layers of Ultrathin Phase Change Material Film. *ACS Photonics* **3**, 1265–1270 (2016).

73. Chen, Y., Li, X., Luo, X., Maier, S. A. & Hong, M. Tunable near-infrared plasmonic perfect absorber based on phase-change materials. *Photonics Res.* **3**, 54 (2015).
74. Rudé, M. *et al.* Ultrafast and Broadband Tuning of Optical Nanostructures using Phase Change Materials. *In preparation* 1–21
75. Huang, Y., Liu, L., Johnson, M., C Hillier, A. & Lu, M. One-step sol-gel imprint lithography for guided-mode resonance structures. *Nanotechnology* **27**, (2016).
76. Johnson, P. B. & Christy, R. W. Optical Constants of the Noble Metals. *Phys. Rev. B* **6**, 4370–4379 (1972).